J. Fluid Mech. (2011), *vol.* 682, *pp.* 617–651. © Cambridge University Press 2011
doi:10.1017/jfm.2011.253

Mean dynamics of transitional boundary-layer flow

J. KLEWICKI[1,2]†, R. EBNER[1] AND X. WU[3]

[1]Department of Mechanical Engineering, University of New Hampshire, Durham, NH 03824, USA
[2]Department of Mechanical Engineering, University of Melbourne, Melbourne, VIC 3010, Australia
[3]Department of Mechanical Engineering, Royal Military College of Canada, Kingston, Ontario, Canada K7K 7B4

(Received 26 January 2011; revised 26 May 2011; accepted 1 June 2011; first published online 19 July 2011)

The dynamical mechanisms underlying the redistribution of mean momentum and vorticity are explored for transitional two-dimensional boundary-layer flow at nominally zero pressure gradient. The analyses primarily employ the direct numerical simulation database of Wu & Moin (*J. Fluid Mech.*, vol. 630, 2009, p. 5), but are supplemented with verifications utilizing subsequent similar simulations. The transitional regime is taken to include both an instability stage, which effectively generates a finite Reynolds stress profile, $-\rho\overline{uv}(y)$, and a nonlinear development stage, which progresses until the terms in the mean momentum equation attain the magnitude ordering of the four-layer structure revealed by Wei *et al.* (*J. Fluid Mech.*, vol. 522, 2005, p. 303). Self-consistently applied criteria reveal that the third layer of this structure forms first, followed by layers IV and then II and I. For the present flows, the four-layer structure is estimated to be first realized at a momentum thickness Reynolds number $R_\theta = U_\infty\theta/\nu \simeq 780$. The first-principles-based theory of Fife *et al.* (*J. Disc. Cont. Dyn. Syst.* A, vol. 24, 2009, p. 781) is used to describe the mean dynamics in the laminar, transitional and four-layer regimes. As in channel flow, the transitional regime is marked by a non-negligible influence of all three terms in the mean momentum equation at essentially all positions in the boundary layer. During the transitional regime, the action of the Reynolds stress gradient rearranges the mean viscous force and mean advection profiles. This culminates with the segregation of forces characteristic of the four-layer regime. Empirical and theoretical evidence suggests that the formation of the four-layer structure also underlies the emergence of the mean dynamical properties characteristic of the high-Reynolds-number flow. These pertain to why and where the mean velocity profile increasingly exhibits logarithmic behaviour, and how and why the Reynolds stress distribution develops such that the inner normalized position of its peak value, y_m^+, exhibits a Reynolds number dependence according to $y_m^+ \simeq 1.9\sqrt{\delta^+}$.

Key words: turbulence theory, turbulent boundary layers, turbulent transition

1. Introduction

As in the channel flow study of Elsnab *et al.* (2011), the *transitional* flat-plate boundary-layer flow of the present investigation is described relative to two

† Email address for correspondence: joe.klewicki@unh.edu

https://doi.org/10.1017/jfm.2011.253 Published online by Cambridge University Press

stages of development. An initial *instability* stage involves the onset and growth of instabilities until the interactions between finite-amplitude fluctuations become self-sustaining. (Note that many researchers view this stage to be synonymous with *transition*.) This is subsequently followed by a *nonlinear development* stage. This stage remains dynamically distinct until the terms in the mean momentum equation evolve to a magnitude ordering that is formally representative of high-Reynolds-number wall turbulence. In the present effort, attention is primarily devoted to the nonlinear development stage; although some discussion of the *instability* stage is also provided. The context for the data presentation, analysis and interpretation is established by briefly describing (i) the physics affiliated with the instability and nonlinear development stages of the transitional regime, (ii) the appropriate dynamical equations (and the dynamics of) the laminar and turbulent regimes bracketing the transitional regime and (iii) elements of a first-principles-based theory that builds upon the mathematical structure of the governing equation in the bounding turbulent regime. This context serves an overarching aim towards developing a mechanistically descriptive and mathematically cogent framework that embraces the dynamical evolution from the laminar regime, through the transitional regime, and into the regime characteristic of high-Reynolds-number boundary-layer flow.

1.1. *Instability and nonlinear development stages*

A central focus is on the emergence, development and dynamical influence of the Reynolds stress gradient, $-\rho\partial\overline{uv}/\partial y$. As revealed via linear stability analysis, a non-zero Reynolds stress first appears near the critical layer of the most unstable disturbances, e.g. Criminale, Jackson & Joslin (2003). Calculations by Jordinson (1970) showed that for supercritical Reynolds numbers the Reynolds stress distribution, $-\rho\overline{uv}(y)$, caused by linear instabilities rapidly evolves to one having a single (positive) sign and a single maximum. These properties persist for all subsequent Reynolds numbers and inherently result in the juxtaposition of positive and negative Reynolds stress gradients interior and exterior to $-\rho\overline{uv}_{max}$, respectively. Jordinson's calculations also indicate that the initial Reynolds stress distributions are spatially localized. For example, for the disturbances he considered, the outer edge of the $-\rho\overline{uv}(y)$ profile only extended to about 0.4δ.

The instability stage of transitional boundary-layer flow exhibits traits common to other wall flows. These include that it occurs over a narrow Reynolds number range, and that the flow is rapidly destabilized by three-dimensional perturbations. This second attribute is consistent with observations that during the later part of the instability stage, the vorticity field undergoes a rapid three-dimensionalization. Rationally, the instability stage melds into the nonlinear development stage once the vorticity fluctuations are finite and three-dimensional.

The physics of the subject flow underlie significant reorganizations of the mean distributions of momentum and vorticity. Attributes of the flow field evolution include a rapid trend towards a spatially uniform distribution of mean momentum, along with a wallward concentration of mean vorticity. Concomitantly, the mean dynamical mechanisms rapidly evolve towards a new and more complex ordering of relative magnitudes across the layer. This process is initiated during the instability stage and completed at the end of the nonlinear development stage. The relative ordering attained at the end of this process underpins scaling descriptions based upon the equations of motion, e.g. Fife *et al.* (2009). Specifically, in the absence of any additional forces, it is readily surmised that, once established, the indicated ordering will not only be maintained, but become increasingly well established for all higher Reynolds

https://doi.org/10.1017/jfm.2011.253 Published online by Cambridge University Press

numbers. Consequently, the scaling behaviours dictated by this ordering also become increasingly well established.

Many wall flows exhibit highly similar behaviours. Boundary layers, however, contain dynamically significant features that are distinct from those in fully developed pipe and channel flows. Primary among these is that boundary layers are spatially developing, and thus have a Reynolds number that increases with downstream fetch. In addition, the mean differential force balance for the boundary layer contains a mean advection term that contributes to the $\mathrm{d}m\boldsymbol{v}/\mathrm{d}t$ part of $\Sigma\boldsymbol{F} = \mathrm{d}m\boldsymbol{v}/\mathrm{d}t$. This term is a non-simple function of both the distance from the wall and Reynolds number. In contrast, the pressure gradient is the analogous term in the mean differential force balance for fully developed pipe and channel flows. At any fixed Reynolds number, this pressure gradient force has a magnitude proportional to the Reynolds number, and has a constant value across the layer. As demonstrated herein, these differences gain apparent significance during the nonlinear development stage.

1.2. *Dynamical mechanisms of the laminar and four-layer regimes*

Our aim here is to explore the mean dynamics of canonical boundary-layer flow, beginning with the first appearance of a finite-Reynolds-stress distribution, and ending at a Reynolds number in which the ordering of terms in the equation of mean dynamics is representative of high-Reynolds-number flows. Towards this aim, it is useful to describe the mean dynamical mechanisms operative in the laminar and fully turbulent flows that bracket the Reynolds number range of interest.

We consider incompressible boundary-layer flow over a planar surface. The mean flow is in the x-direction, and y is normal to the wall. Consistent with convention, the disturbance thickness of the boundary layer is given by $\delta = \delta_{99} = \delta(x)$. The velocity components in the x- and y-directions are given by variants of u and v, respectively. A tilde denotes an instantaneous quantity, and an uppercase or an overbar denotes time-averaged quantities. Fluctuations about the mean are denoted by lowercase letters.

In the case of the steady laminar flat-plate boundary layer, Prandtl's boundary-layer equation reduces to

$$\rho\left(\tilde{u}\frac{\partial\tilde{u}}{\partial x} + \tilde{v}\frac{\partial\tilde{u}}{\partial y}\right) = \mu\frac{\partial^2\tilde{u}}{\partial y^2}, \tag{1.1}$$

where μ is the dynamic viscosity. Equation (1.1) indicates that the time-rate-of-change of momentum (left-hand side) everywhere results from a retarding viscous stress gradient (right-hand side). The balance of (1.1) is graphically represented by plotting the ratio of its functions versus position from the wall. This graph simply consists of a horizontal line at -1 extending from $y = 0$ to $y = \delta$. A -1 ratio of terms also characterizes the balance in the fully developed laminar channel flow. In contrast, however, the functions associated with (1.1) vary considerably across the layer (see figure 7*a*), while in laminar channel flow the individual terms in the differential momentum balance are constant.

For the turbulent case the flow is statistically stationary, and thus the mean dynamics is described by the Reynolds-averaged boundary-layer equation. The appropriately simplified form of this equation is

$$\rho\left(U\frac{\partial U}{\partial x} + V\frac{\partial U}{\partial y} + \frac{\partial\overline{uv}}{\partial y}\right) = \mu\frac{\partial^2 U}{\partial y^2}. \tag{1.2}$$

https://doi.org/10.1017/jfm.2011.253 Published online by Cambridge University Press

Time averaging of turbulent flow leads to an additional and unknown term arising from the net correlation between the u and v velocity fluctuations – the so-called Reynolds shear stress. (Note that the semi-empirical analyses of Monkewitz, Chauhan & Nagib 2008 and the direct numerical simulation (DNS) data sets of the present study indicate that potential contributions from the streamwise gradients of the normal turbulent stresses are negligible.) Somewhat contrary to convention, the gradient of the Reynolds stress is shown as the last term on the left-hand side of (1.2). This is done to reinforce the fact that the Reynolds stress gradient is the net time-averaged effect of turbulent inertia. It is similarly worth noting that even in transitional and turbulent boundary-layer flows the ratio of the total mean inertia (mean advection plus turbulent inertia) to the mean viscous force also equals -1 at every point across the layer. In turbulent pipe and channel flows, a segregation of the terms into forces and inertia reveals that the momentum balance is characterized by the sum of two forces (viscous stress gradient plus pressure gradient) equalling a single inertial mechanism (Reynolds stress gradient).

As now demonstrated, there are good reasons to consider the contributions of the Reynolds stress gradient as a separate dynamical effect. The time-mean statement of dynamics is given in inner-normalized form in (1.3), where a superscript $+$ denotes normalization by the kinematic viscosity, $\nu = \mu/\rho$, and the friction velocity, $u_\tau = \sqrt{\tau_w/\rho}$, where τ_w is the mean wall shear stress and ρ is the mass density. Three mechanisms are apparent in (1.3): A = inertia of the mean flow (mean advection), B = mean viscous force (gradient of the viscous stress) and C = average effect of turbulent inertia (gradient of the Reynolds stress).

$$\left.\begin{aligned} 0 &= -\left(U^+\frac{\partial U^+}{\partial x^+} + V^+\frac{\partial U^+}{\partial y^+}\right) + \frac{\partial^2 U^+}{\partial y^{+2}} - \frac{\partial \overline{uv}^+}{\partial y^+}, \\ 0 &= \qquad\qquad \mathrm{A} \qquad\qquad + \quad \mathrm{B} \quad + \quad \mathrm{C} \end{aligned}\right\} \tag{1.3}$$

The ratio of any two terms exposes how the balance expressed by (1.3) is realized. Given the high-Reynolds-number ordering of terms in turbulent wall flows, this is generally best accomplished by examining the ratio of term B to term C (e.g. see Wei *et al.* 2005*a*; Klewicki *et al.* 2007; Fife *et al.* 2009). Figure 1 displays a schematic representation of the ratio of terms B/C in (1.3) at fixed Reynolds number in the fully turbulent regime. This sketch effectively reflects the mean free-body diagram for the differential fluid elements at each position within the layer. A non-trivial balance can occur owing to either two or three co-dominant terms. The balance of (1.3) is attained according to a different ordering in four distinct layers: layer I, $|A| \simeq |B| \gg |C|$; layer II, $|B| \simeq |C| \gg |A|$; layer III $|A| \simeq |B| \simeq |C|$; layer IV, $|A| \simeq |C| \gg |B|$ (e.g. Wei *et al.* 2005*a*). Relative to layer I, Wei *et al.* (2005*a*) note that its thickness is less than that in the channel, and the present data and those of Schlatter & Orlu (2010) provide evidence that in the zero-pressure-gradient boundary layer the stress gradient balance layer (layer II) may extend all the way to the wall – as it does in Couette flow. This has to do with the rates at which the terms in (1.3) tend to zero as $y^+ \to 0$. On the other hand, for flow in pressure-driven channels (or pipes), it is easily shown that a layer exists next to the wall within which the mean viscous stress gradient and mean pressure gradient balance to leading order. The reader is referred to Wei, Fife & Klewicki (2007) for additional details regarding the nature of the force balance in and near layer I.

https://doi.org/10.1017/jfm.2011.253 Published online by Cambridge University Press

Physical layer	Δy increment	ΔU increment
I	$O(\nu/u_\tau)$ ($\lesssim 3$)	$O(u_\tau)$ ($\lesssim 3$)
II	$O(\sqrt{\nu\delta/u_\tau})$ ($\simeq 1.6$)	$O(U_\infty)$ ($\simeq 0.5$)
III	$O(\sqrt{\nu\delta/u_\tau})$ ($\simeq 1.0$)	$O(u_\tau)$ ($\simeq 1$)
IV	$O(\delta)$ ($\to 1$)	$O(U_\infty)$ ($\to 0.5$)

TABLE 1. Scaling behaviours of the layer thicknesses and velocity increments associated with the mean momentum equation (see figure 1). Note that the layer IV properties are asymptotically attained as $\delta^+ \to \infty$, after Klewicki *et al.* (2007).

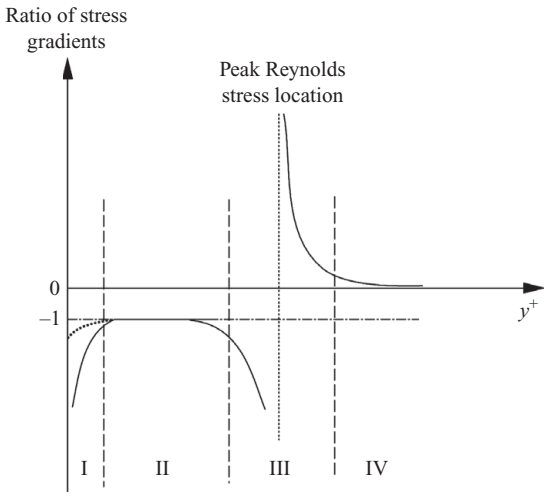


FIGURE 1. Sketch of the ratio of terms B/C revealing the four-layer force balance structure of turbulent wall-bounded flows at a fixed Reynolds number (adapted from Wei *et al.* 2005*a*). Note that layer I in the zero-pressure-gradient turbulent boundary layer is different from that of the channel and pipe flows in that in this case all of the terms in the time-averaged momentum equation approach zero as $y \to 0$.

The scaling behaviours associated with the thicknesses and the velocity increments across each layer have been determined (e.g. see Wei *et al.* 2005*a*; Klewicki *et al.* 2007). For future reference, these are summarized in table 1.

1.3. *Mean flow theory*

As demonstrated by the channel flow study of Elsnab *et al.* (2011), the mean flow theory developed by Fife *et al.* (2009) provides a useful framework for connecting the laminar, transitional and four-layer regimes. Although analogous to that of the fully developed channel flow, the boundary-layer equation analysis is complicated by an x-dependence and, more significantly, by the non-constancy of the mean advection profile in (1.3) over $0 \leqslant y \leqslant \delta$. Consequently, the results for the channel are realized in a more exact and explicit form. Primary mathematical features are, however, retained. Elements of these are now succinctly described.

With minimal loss of generality, one can write (1.3) as

$$\frac{\partial^2 U^+}{\partial y^{+2}} + \frac{\partial T^+}{\partial y^+} + \epsilon^2 b = 0, \tag{1.4}$$

https://doi.org/10.1017/jfm.2011.253 Published online by Cambridge University Press

where $\epsilon = \epsilon(x^+)$, $b = b(x^+, y^+, \epsilon)$ and, to be consistent with previous publications, $T^+ = -\overline{uv}^+$ is employed. The unknown $O(1)$ function b is constrained such that $\int_0^{\delta^+} b\,\mathrm{d}y^+ = O(\delta^+)$ for all ϵ. Given this, integration of (1.4) yields $\epsilon^{-2}(x^+) = O(\delta^+)$. Thus, under this generic construction, the unknown function b predominantly captures the shape of the mean advection profile, and ϵ effectively captures its Reynolds number variation. As noted by Metzger, Adams & Fife (2008), no derivatives with respect to x explicitly appear in (1.4) or its boundary conditions. Thus, as in their approach, x^+ is treated as a parameter, so that the properties deduced for U^+ and T^+ are taken to be valid at any given x^+. This approach finds empirical support from the Reynolds number dependence of U_∞^+ in equilibrium boundary layers, as well as from the close correspondence between the observed properties of the four-layer structure in pipes, channels and boundary layers (Wei *et al.* 2005*a*; Metzger *et al.* 2008). These considerations imply that (1.4) is well approximated by

$$\frac{\mathrm{d}^2U^+}{\mathrm{d}y^{+2}} + \frac{\mathrm{d}T^+}{\mathrm{d}y^+} + \epsilon^2 b(y^+, \epsilon) = 0. \tag{1.5}$$

Following the methodology described by Fife *et al.* (2009), (1.5) can be shown to admit an invariant form on each of a continuous hierarchy of internal scaling layers, L_β. The position and width of each member of the L_β hierarchy is determined by the small parameter β, which depends upon the decay rate of the Reynolds stress gradient. This is shown by invoking the transformation

$$T_\beta(y^+) = T^+(y^+) - T^*(\eta, \epsilon) - \beta y^+, \tag{1.6}$$

where $\eta = \epsilon^2 y^+ = O(y/\delta)$. In (1.6), $T^*(\eta, \epsilon)$ is the outer approximation to the Reynolds stress,

$$T^* = \int_\eta^{\eta(\delta)} b(s, \epsilon)\,\mathrm{d}s, \tag{1.7}$$

where $\eta(\delta)$ denotes the value of η at $y = \delta$, which is an $O(1)$ quantity. Substitution of (1.6) into (1.5) yields

$$\frac{\mathrm{d}^2U^+}{\mathrm{d}y^{+2}} + \frac{\mathrm{d}T^+}{\mathrm{d}y^+} + \beta = 0, \tag{1.8}$$

which is of a form identical to that found for channel flow (Fife *et al.* 2005*a*).

An important property of the L_β hierarchy is that across each constituent layer there is a balance breaking and exchange of terms analogous to that occurs across layer III in figure 1. That is, for each value of β, the T_β function attains a maximum value, $T_{\beta m}$, at a position $y_m^+(\beta)$ on the hierarchy, with $y_m^+(\beta)$ increasing as β decreases. As with layer III, each layer on the hierarchy is nominally centred about the corresponding $y_m^+(\beta)$. On each L_β layer (and on layer III), all three terms in (1.8) are of the same order of magnitude. This fact motivates a rescaling of (1.8) that formally renders all terms $O(1)$ independent of δ^+. Differential transformations of the form

$$\mathrm{d}y^+ = \beta^{-1/2}\mathrm{d}\hat{y}, \quad \mathrm{d}T_\beta = \beta^{1/2}\mathrm{d}\hat{T}, \quad \mathrm{d}U^+ = \mathrm{d}\hat{U} \tag{1.9}$$

accomplish this task, and yield the invariant form

$$\frac{\mathrm{d}^2U^+}{\mathrm{d}\hat{y}^2} + \frac{\mathrm{d}\hat{T}}{\mathrm{d}\hat{y}} + 1 = 0, \tag{1.10}$$

which is operative on every layer of the L_β hierarchy.

https://doi.org/10.1017/jfm.2011.253 Published online by Cambridge University Press

As to the developments leading to (1.10), it is important to note some distinctive differences with channel flow. Because the pressure gradient is independent of y, the outer approximation for T^+ for channel flow can be written as an explicit function of y/δ. On the other hand, examination of (1.6) and (1.7) reveals that determining β in the boundary layer requires evaluation of an integral of the mean advection function, b, whose order of magnitude properties are known, but whose detailed features are unknown. The channel flow result ultimately leads one to expect the $U^+(y^+)$ profile to approach an exactly logarithmic form as $\delta^+ \to \infty$ (Fife *et al.* 2009). The logarithmic approximation in the boundary layer is also expected to improve as $\delta^+ \to \infty$. The variable nature of b, however, provides good reason to doubt that the asymptotic profile is exactly logarithmic. Another implication relates to the properties of the L_β width distribution, $W(y^+)$, as $\delta^+ \to \infty$. In either case, $W(y^+)$ approaches a linear function on the hierarchy. Apparently, owing to the constancy of the pressure gradient function across the channel, the slope of $W(y^+)$ can be explicitly related to the leading coefficient, $4/A(\beta)^2$, of the logarithmic profile equation,

$$U^+ = \frac{4}{A^2}\ln(y^+ - C) + D, \tag{1.11}$$

where $A(\beta)$ is given by (1.12), and C and D are constants. This analytical result was first found by Fife *et al.* (2005*b*). Somewhat surprisingly, these order-of-magnitude estimates were later shown to gain both qualitative and precise quantitative support from channel DNS data (Klewicki, Fife & Wei 2009). (Note that if one calls the leading coefficient $1/\kappa$, then this result is expressed as $\mathrm{d}W/\mathrm{d}y^+ = \sqrt{\kappa}$.) In the case of the approximate formulation for the boundary layer (1.5), the relationship between the slope of the increasingly linear $W(y^+)$ profile and the leading coefficient cannot be made explicit. This matter is further discussed in § 3.5.2.

A direct consequence of the differential transformations (1.9) leading to the invariant form of the mean momentum equation (1.10) is that when normalized using the scales local to the given member of the L_β hierarchy, the curvature of the Reynolds stress evaluated at each $y_m^+(\beta)$ ($\hat{y} = 0$) becomes an $O(1)$ quantity, $A(\beta)$, i.e.

$$A(\beta) = -\frac{\mathrm{d}^2\hat{T}}{\mathrm{d}\hat{y}^2}(\hat{y} = 0). \tag{1.12}$$

Although $A(\beta)$ is ensured to remain $O(1)$ on the L_β hierarchy, it is further expected to approximate constancy on an interior domain of the hierarchy and exhibit decreasing variation as $\delta^+ \to \infty$. Over the range of wall-normal distances where this occurs, the mean profile develops an approximately logarithmic profile, with the accuracy of the approximation improving as $\delta^+ \to \infty$ (Fife *et al.* 2009). Recent analyses of channel flow DNS support these analytical predictions (Klewicki *et al.* 2009).

Fundamentally, (1.12) is a statement about a specific dynamical self-similarity that develops on the L_β hierarchy, and that is realized with increasing accuracy as the Reynolds number becomes large. For the boundary layer, (1.12) implicitly includes the dependence of β on the mean advection profile. This is made explicit in the expression that relates the inner normalized second derivative of the Reynolds stress to $A(\beta)$,

$$\frac{\mathrm{d}^2T^+(y_m^+(\beta))}{\mathrm{d}y^{+2}} = -A(\beta)\beta^{3/2} - \epsilon^2\frac{\mathrm{d}b(y_m^+(\beta))}{\mathrm{d}\beta}, \tag{1.13}$$

where is it useful to note that $y_m^+(\beta)$ corresponds to $\hat{y} = 0$ for each β (e.g. see Metzger *et al.* 2008, Appendix A).

https://doi.org/10.1017/jfm.2011.253 Published online by Cambridge University Press

1.4. *Objectives*

An overarching goal of the present investigation is to expose how the simple laminar flow force balance, expressed by the -1 ratio of terms in (1.1), evolves to the four-layer structure depicted in figure 1. The physical and mathematical implications are exposed within the context of the theory just described. Per the considerations discussed above, important elements of the present study include clarifying how and at what post-instability Reynolds number the ordering of the terms in the mean statement of dynamics becomes representative of the high-Reynolds-number flow, as well as clarifying the predominant differences between the mean dynamics of transitional flow in the boundary layer and the channel.

2. Data sets

The analyses primarily utilize data from the DNS of Wu & Moin (2009), but with key comparisons with the simulations of Wu & Moin (2010) and Wu (2010). These comparisons explore the sensitivity of the results to the method by which the boundary-layer instabilities are triggered. The simulation of Wu & Moin (2009) employed a finite-difference formulation to solve the Navier–Stokes equations on a grid having 4096 points in the streamwise (x) direction, 400 points in the wall-normal (y) direction and 128 points in z. The simulation of Wu & Moin (2010) employed a finite-difference formulation on a grid having 8192, 500 and 256 points in the x-, y- and z-directions, respectively. The simulation of Wu (2010) utilized a grid having 8192, 500 and 256 points.

The simulations used here compute spatially developing flow fields, and thus they do not rely on a recycling of the outflow. Simulations of this type do, however, require a triggering of the transition process. For the simulations of Wu & Moin (2009) and Wu & Moin (2010) transition was initiated by advecting patches of free-stream turbulence introduced at regular intervals at the inflow boundary. Relative to the simulations of former, the patches in the latter are doubled in size in order to maintain mean homogeneity in the spanwise direction. For the simulation of Wu (2010), transition is initiated through the use of turbulent wakes advecting at an angle of 35° with respect to the $y=0$ plane. In all three cases, the advecting disturbances trigger instabilities in accordance with the receptivity of the base laminar flow. Based upon the nature of these perturbations, the simulation of Wu & Moin (2009) is viewed to be the most delicately triggered, while the simulation of Wu (2010) is deemed to initiate instabilities most aggressively. As discussed below, the specific processes associated with these disturbances are likely to influence the initial width of the Reynolds stress distribution during the instability stage. For example, the simulations of Schlatter & Orlu (2010) show highly similar results (e.g. see § 3.4.3), even though they used a body force disturbance to trigger instabilities. For more details regarding other aspects of the present simulations, refer to Wu & Moin (2009, 2010) and Wu (2010).

3. Results

3.1. *Mean flow behaviours*

Inner normalized profiles of the mean velocity and Reynolds stress are given in figure 2(a,b), respectively, for $35 \lesssim \delta^+ (= \delta u_\tau/\nu) \lesssim 370$. As is apparent from the conventional semi-logarithmic plot of U^+ versus y^+, for $\delta^+ \gtrsim 150$, the mean profile

https://doi.org/10.1017/jfm.2011.253 Published online by Cambridge University Press

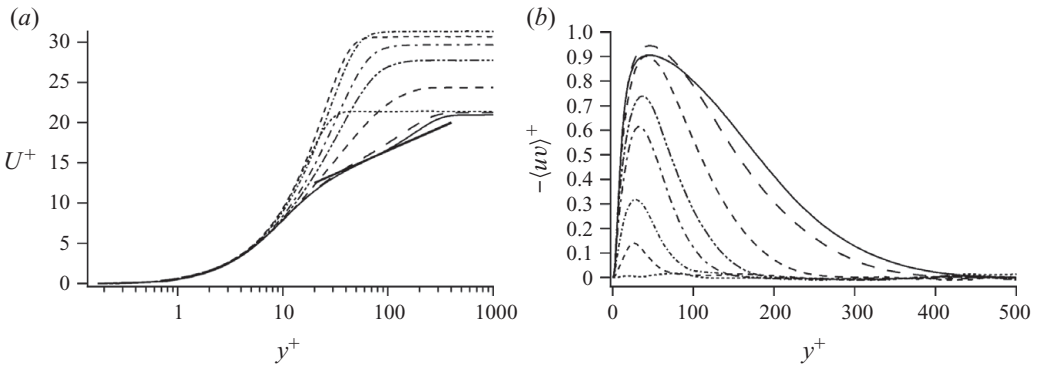


FIGURE 2. Mean velocity and Reynolds stress profiles from the simulation of Wu & Moin (2009). (*a*) Inner normalized mean velocity versus inner normalized distance from the wall and (*b*) inner normalized Reynolds stress versus outer normalized distance from the wall. Line styles throughout are as follows: . . . , $\delta^+ \simeq 35$ ($R_\theta = 100$); - - -, $\delta^+ \simeq 58$ ($R_\theta = 225$); - · -, $\delta^+ \simeq 76$ ($R_\theta = 280$); — - —, $\delta^+ \simeq 111$ ($R_\theta = 350$); — - -, $\delta^+ \simeq 144$ ($R_\theta = 400$); — — —, $\delta^+ \simeq 211$ ($R_\theta = 500$); — —, $\delta^+ \simeq 327$ ($R_\theta = 700$); —, $\delta^+ \simeq 367$ ($R_\theta = 800$). The dark solid line has a slope of 2.5.

rapidly changes shape towards one becoming more identifiable with turbulent flow. By $\delta^+ \simeq 370$, the U^+ profile shows evidence of an emerging logarithmic zone with a slope of about 2.8. For reference, a line having a constant slope of 2.5 is included in this plot.

The $-\overline{uv}^+$ profiles of figure 2(*b*) emerge as a small, internally localized, bump. Linear stability theory indicates that the first appearance of the Reynolds stress (and thus its gradient) is spatially localized near the critical layer associated with the most unstable disturbance, e.g. Criminale *et al.* (2003). Jordinson (1970) showed that the Reynolds stress profiles for disturbances at both subcritical and early supercritical Reynolds numbers exhibit a positive peak near the critical layer and a negative excursion in the outer region of the boundary layer. For subcritical Reynolds numbers, this region is described by Jordinson as one of negative turbulence production, and is seen to underlie the decay of the disturbance field. For increasing supercritical Reynolds numbers, this region of negative $-\overline{uv}^+$ diminishes and the flow proceeds through the instability stage and into the nonlinear development stage. A close examination of the $\delta^+ \simeq 35$ profile of figure 2(*b*) reveals that the outer region $-\overline{uv}^+$ profile exhibits a zone of small negative values. Linear theory predicts that the onset of instability, *indifference point* as described by Schlichting & Gersten (2000), occurs near $R_\theta = U_\infty \theta / \nu = 200$ (θ = momentum deficit thickness), or equivalently $\delta^+ \simeq 50$. Thus, for the lower Reynolds numbers the present Reynolds stress distributions result from finite perturbations of a subcritical flow. Furthermore, the relatively broad distribution of the nascent Reynolds stress profile (as opposed to a delta-function-like spike) is likely to be associated with the more broadband nature of the initiating disturbances. Elsnab *et al.* (2011) provide additional reasons to expect that the width of the Reynolds stress profile at the onset of the nonlinear development stage is sensitive to the distribution of linear modes excited during the instability stage. In the present case, remnants of the tripping mechanism are evidenced by the random patches of non-zero Reynolds stress in the free stream at the lowest Reynolds numbers. Overall, however, the combined studies of Wu & Moin (2009, 2010) and Wu (2010) provide evidence that the subsequent nonlinear flow field evolution increasingly proceeds in a manner representative of a naturally tripped flow. As indicated by figure 2(*b*) the

https://doi.org/10.1017/jfm.2011.253 Published online by Cambridge University Press

Reynolds stress development through the transitional regime is marked by a rapid increase in magnitude, along with a spreading both towards the wall and the free stream. This spreading of non-zero $-\overline{uv}^+$ towards the periphery gains significance when considering $-\partial\overline{uv}^+/\partial y^+$, and is especially prevalent at low δ^+ (see §§ 3.4.1 and 3.5.3). Comparison of the $\delta^+ \simeq 327$ and 367 profiles provides evidence that near the end of the nonlinear development stage the maximal value of $-\overline{uv}^+$ exhibits an overshoot. This may have connection to the fact that over a narrow δ^+ range, the skin friction (and thus u_τ) has the same value for two different turbulent flows (see figure 4).

Comparison (not shown) indicates that the mean profiles from the simulations of Wu & Moin (2010) and Wu (2010) are qualitatively similar, but different in detail, to the progression of profiles in figure 2(*a*). More significantly, the Reynolds stress profiles from Wu (2010) exhibit a substantial negative excursion in and near the free stream. This negative portion, caused by the passing wakes, diminishes in magnitude with increasing δ^+ until the profiles for $\delta^+ \gtrsim 300$ look very similar to those in figure 2(*b*). Comparatively, the Reynolds stress profiles from the simulation of Wu & Moin (2010) are more similar to those in figure 2(*b*).

In the four-layer regime of figure 1, the inner normalized widths of layers II and III increase at a rate approximately proportional to $\sqrt{\delta^+}$ (see table 1). This proportionality is increasingly well approximated as $\delta^+ \to \infty$. These known scaling behaviours underlie the development of the dominant features of the solutions to the mean momentum equation, i.e. $U^+(y^+)$ and $-\overline{uv}^+(y^+)$. From layer II, across layer III, and into layer IV there is a *balance breaking and exchange* of forces from which the inertial terms (A and C) in (1.3) increasingly gain leading-order importance in layer IV. A central attribute of the structure of figure 1 is that the mean viscous force (term B) retains dominant order to the outer edge of layer III. As discussed in detail by Klewicki *et al.* (2007), consideration of the balance of terms in (1.3) reveals that the mean viscous force manifests itself distinctly differently from that described within the traditional sub-, buffer-, log- and wake-layer framework (also see Eyink 2008).

Further analyses show that the balance breaking and exchange of forces is not only reflected in the overall structure of the mean momentum equation, but that this equation formally admits this structure on each of the continuous hierarchy of internally situated scaling layers described in § 1.3. Each member of the L_β hierarchy is shown to have a construction that is qualitatively the same as layer III. Layer III is on the hierarchy, and, in fact, can be viewed as the average member of the hierarchy. When the length scale intrinsic to a given member of the layer hierarchy is employed, the mean momentum equation admits the invariant form (1.10), and thus yields a universal solution. Significant attributes pertain to the curvature of the $-\overline{uv}^+$ profile on the hierarchy, as well as the inner and outer inflection points that exist in the Reynolds stress profile of this and other turbulent wall flows. These issues are examined in detail in § 3.5. In this context, it is pertinent to note that the $-\overline{uv}^+$ profile is a solution to (1.3), and that during the nonlinear development stage the boundary-layer Reynolds stress profile establishes a characteristic shape and sequence of curvatures that remain the same for all higher δ^+.

An important trait affiliated with the above considerations is that the inner normalized maximal position, y_m^+, of the $-\overline{uv}^+$ distribution adheres to the scaling $y_m^+ \sim \sqrt{\delta^+}$ (Fife *et al.* 2005*a*, 2009). Of course, this scaling behaviour for y_m^+ has also been reasoned to occur and empirically observed by a number of researchers (e.g. Long & Chen 1981; Afzal 1982; Antonia *et al.* 1992; Ching, Djendi & Antonia 1995; Sreenivasan & Sahay 1997; Wei *et al.* 2005*a*). Examination of the literature reveals that y_m^+ scales like $\lambda\sqrt{\delta^+}$. Perhaps the most comprehensive data analyses for

https://doi.org/10.1017/jfm.2011.253 Published online by Cambridge University Press

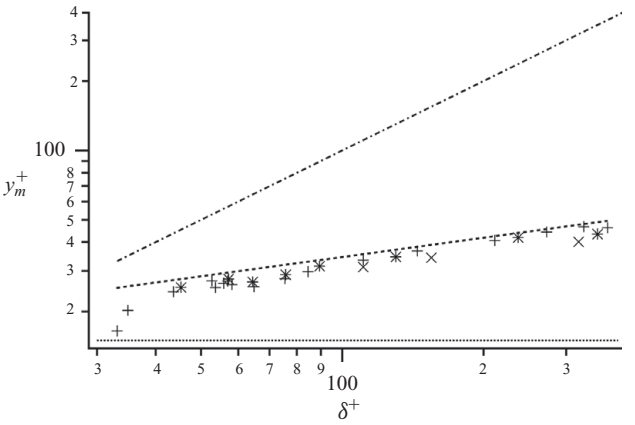


FIGURE 3. Inner normalized position, y_m^+, of the maximum of $-\overline{uv}^+$ as a function of δ^+: +, simulation of Wu & Moin (2009); ×, Wu & Moin (2010); *, Wu (2010). Ascending magnitude lines respectively correspond to rates of the variation associated with the $O(1)$, $O(\sqrt{\delta^+})$ (actually $1.8\sqrt{\delta^+}$) and $O(\delta^+)$ scaling trends.

Reynolds numbers in the four-layer regime have been made by Sreenivasan (1989) and Sreenivasan & Sahay (1997). They found that $\lambda = 1.8 \pm 0.2$, with little discernible effect attributable to whether the flow is a boundary layer, pipe or a channel.

Figure 3 plots y_m^+ versus δ^+ on logarithmic axes for the three DNS explored. For reference, scaling lines proportional to the inner (ν/u_τ), intermediate ($\sqrt{\nu\delta/u_\tau}$) and outer (δ) lengths are also represented in this figure. Note also that since the data are inner normalized, these scalings appear as lines following $y_m^+ \sim 1$, $\sqrt{\delta^+}$ and δ^+, respectively. Through the instability stage y_m^+ exhibits a rapid increase with δ^+. Similar behaviours were observed in the channel flow study by Elsnab *et al.* (2011). In all cases, the $-\overline{uv}^+$ profile rapidly broadens during the instability stage to generate non-zero $-\partial\overline{uv}^+/\partial y^+$ over essentially the entire flow domain. The data from the simulations of Wu & Moin (2009) and Wu (2010) show a small range of δ^+ ($45 \lesssim \delta^+ \lesssim 80$), over which the rate of increase in y_m^+ is intermediate to inner and outer scaling, but noticeably less than $\sqrt{\delta^+}$. The development of y_m^+ with δ^+ in channel flow also exhibits this trait (Elsnab *et al.* 2011). Examination of figures 2(*b*) and 4 indicates that this slower rate nominally begins when the skin friction discernibly breaks from the laminar line, and nominally terminates when the gradient of $-\overline{uv}^+$ no longer spreads inwards – presumably owing to the constraints posed by the wall boundary condition. For all of the cases plotted, y_m^+ increases at a rate that is intermediate to inner and outer scaling. For $\delta^+ \gtrsim 80$, the y_m^+ data trend outward at a rate close to $\sqrt{\delta^+}$. At higher δ^+, the data of DeGraaff & Eaton (2000) (not shown) indicate that $y_m^+ \sim \sqrt{\delta^+}$ (see Wei *et al.* 2005*a*). Overall, the results of figure 3 are consistent with the notion that the mean flow properties of the early nonlinear development stage have some sensitivity to the details of the instability stage. With increasing δ^+, however, nonlinear interactions gain increasing dominance, and the robust features affiliated with the four-layer regime emerge.

3.2. *Skin friction*

The C_f profile from Wu & Moin (2009) of figure 4 discernibly breaks from the laminar curve near $\delta^+ = 50$ ($R_\theta = U_\infty\theta/\nu \simeq 200$), and subsequently rises up to the curve described by empirical correlations at $R_\theta \simeq 780$ ($\delta^+ \simeq 360$). These behaviours

https://doi.org/10.1017/jfm.2011.253 Published online by Cambridge University Press

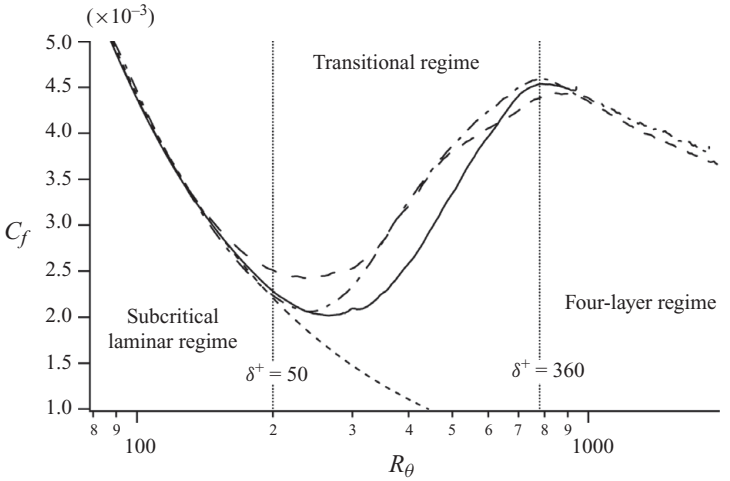


FIGURE 4. Skin-friction coefficient for present boundary layer results as a function of the Reynolds number: - - -, laminar theory; —, Wu & Moin (2009); — — —, Wu & Moin (2010); — - —, Wu (2010).

are significant on a number of counts. The analysis of the stress gradient ratios in § 3.4.3 reveals that this Reynolds number range effectively bounds the nonlinear development stage of the present boundary layer flows, as the four-layer regime of figure 1 is first attained at $\delta^+ \simeq 360$. This behaviour is qualitatively distinct from channel flow. For example, the C_f rise to the empirical curves for boundary layers (a number of which are given in Nagib, Chauhan & Mokewitz 2007) apparently occurs over a broader δ^+ range than in the channel. Thus, as indicated by comparing figures 4 and 5, the four-layer regime for boundary layers appears to begin at the end of the rise in C_f.

In planar Poiseuille flow the skin-friction coefficient, $C_f = \tau_w/(1/2\rho U_\infty^2)$, undergoes an abrupt increase by increasing δ^+ through the instability stage. C_f jumps from the strongly decreasing laminar line (in that case a power law of constant negative slope) to a curve that is approximately described by any of a number of empirical correlations (e.g. Dean 1978). As δ^+ is increased further, subsequent decreases along the C_f curve occur much more slowly than along the laminar C_f line. In the channel, the flow develops over a significant δ^+ range along this new curve ($65 \lesssim \delta^+ \lesssim 180$) prior to the terms in the mean momentum equation attaining the magnitude ordering representative of the four-layer regime. These features are depicted in figure 5. As described below, these differences between channel and boundary-layer flows are associated with the slower rate at which mean vorticity concentrates nearer to the wall in the boundary layer, and the interplay between the inertia of the mean flow (mean advection) and the net mean effect of turbulent inertia (Reynolds stress gradient).

For comparison, figure 4 also shows the C_f versus R_θ profile from the laminar theory associated with the Blasius profile, and from the simulations of Wu & Moin (2010) and Wu (2010). Regarding the former, it is worth noting that the DNS C_f curves approximately follow the laminar line for a significant Reynolds number range after the first appearance of a finite Reynolds stress gradient; occurring at about $R_\theta = 100$ ($\delta^+ \simeq 35$) (see figure 7*a*, *b*). (Also bear in mind that the simulations of Wu & Moin 2009 and Wu & Moin 2010 are rendered unstable through the imposition of finite three-dimensional free-stream disturbances, while turbulence in the simulation

https://doi.org/10.1017/jfm.2011.253 Published online by Cambridge University Press

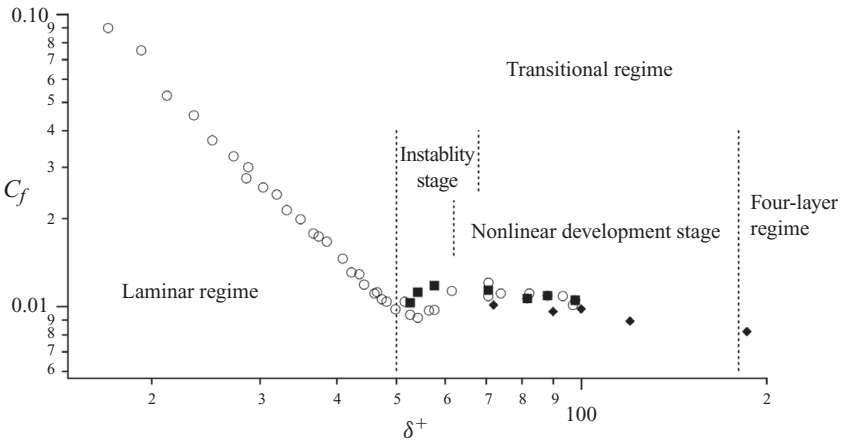


FIGURE 5. Skin-friction coefficient for channel flow as a function of the Reynolds number: ○, pressure drop based data of Elsnab *et al.* (2010); ■, Reynolds-stress integral-based results of Elsnab *et al.* (2011); ◆, DNS data of Kuroda, Kasagi & Hirata (1989), Laadhari (2002) and Hoyas & Jimenez (2006). Figure adapted from Elsnab *et al.* (2011).

of Wu 2010 is triggered by passing wakes.) All of these DNS curves are qualitatively similar, but with some quantitative differences.

3.3. *Mean vorticity field development*

As δ^+ increases through the transitional regime, an increasingly greater fraction of the mean vorticity, $\Omega_z \simeq -\partial U/\partial y$, concentrates nearer to the wall. Commensurate with the eventual development of a logarithmic mean velocity profile, this wallward concentration occurs in concert with the formation of a low-amplitude and relatively slowly decreasing (with increasing y^+) outer region Ω_z profile.

The initial rate at which the mean vorticity concentrates nearer to the surface is significantly slower in the boundary layer than in the channel. This fact is quantified by comparing the development of the displacement thickness, δ^*. Physically, the displacement thickness

$$\delta^* = \int_0^\delta \left(1 - \frac{U}{U_\infty}\right) \mathrm{d}y \simeq \frac{\displaystyle\int_0^\delta y\Omega_z \,\mathrm{d}y}{\displaystyle\int_0^\delta \Omega_z \,\mathrm{d}y} \tag{3.1}$$

measures the distance from the wall to the centroid of the mean vorticity, e.g. Sherman (1990). The second expression in (3.1) is exact in channel flow and commensurate with the boundary-layer approximation, since for the boundary layer $|\partial U/\partial y| \gg |\partial V/\partial x|$. Figure 6 presents δ^*/δ versus δ^+ from the present data sets, the $\delta^+ = 251$ and 361 data of Schlatter & Orlu (2010), as well as for channel flow. (Note that in the channel flow, δ signifies the half-channel height.) These data indicate that for $35 \lesssim \delta^+ \lesssim 370$ the centroid of the mean vorticity moves closer to the wall by over a factor of two; from slightly greater than $\delta/3$ to about $\delta/6$. The slower rate of wallward Ω_z concentration is plausibly associated with the fact that δ grows in the boundary layer, but is fixed in the channel. There is also the active process of vorticity annihilation near the centreline of the channel. Of course, these factors also connect to the rather dramatic rearrangement of the mean advection profile through the nonlinear development stage

https://doi.org/10.1017/jfm.2011.253 Published online by Cambridge University Press

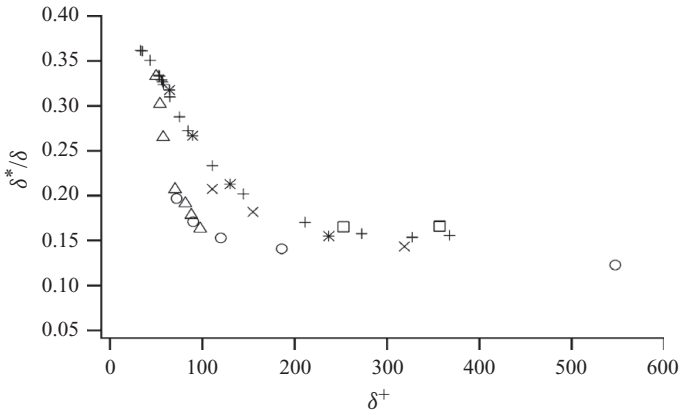


FIGURE 6. Outer normalized displacement thickness as a function of δ^+: +, simulation of Wu & Moin (2009); ×, Wu & Moin (2010); *, Wu (2010); □, Schlatter & Orlu (2010); △, experimental channel data of Elsnab *et al.* (2011); ○, DNS channel data of Laadhari (2002) ($\delta^+ = 72, 90$ and 120) and Hoyas & Jimenez (2006) ($\delta^+ = 186$ and 547).

(see figure 7*a–i*). By the end of their respective nonlinear development stages, the rate of decrease in δ^*/δ is similar for both channel and boundary-layer flows.

3.4. *Evolution of the mean dynamical mechanisms*

The Reynolds-number-dependent features of the mean dynamical mechanisms are first explored by examining the behaviour of the individual terms in (1.3), and then by comparing their relative magnitudes using the ratio of terms as in figure 1. By applying criteria relating to these ratios, we subsequently estimate the δ^+ value that marks the onset of the four-layer regime.

3.4.1. *Balance of terms*

Figure 7(*a–i*) shows the progression of the terms (A, B and C) in (1.3) from the simulation of Wu & Moin (2009) for $35 \lesssim \delta^+ \lesssim 330$ ($80 \lesssim R_\theta \lesssim 700$). As indicated in figure 7(*a*), the nearly laminar balance between mean advection and the viscous stress gradient is attained by functions whose peak amplitudes are located at about 0.6δ. The Reynolds stress gradient rapidly intensifies during the nonlinear development stage. When viewed as a force, this function is characterized by its momentum source-like and sink-like behaviours for $y^+ < y_m^+$ and $y^+ > y_m^+$, respectively (Fife *et al.* 2005*b*; Wei *et al.* 2005*a*; Guala, Hommema & Adrian 2006; Klewicki *et al.* 2007; Ganapathisubramani 2008). Consistent with the $-\overline{uv}^+$ profiles of figure 2, non-zero $-\partial\overline{uv}^+/\partial y^+$ first appears in a spatially localized internal region, and with increasing δ^+ spreads both towards the wall and the free stream. The data of figure 3 quantify that the first detectable peak in $-\overline{uv}^+$ is positioned at $y^+ \simeq 15$. As indicated in figure 7(*b–d*), during the early portion of the nonlinear development stage, the mean advection and Reynolds-stress gradient terms positively sum to balance the negative mean viscous stress gradient for $y^+ < y_m^+$, while the Reynolds and viscous stress gradient terms negatively sum to balance positive mean advection for $y^+ > y_m^+$. (Recall that y_m^+ is given by the zero crossing in the Reynolds-stress gradient profile.) With increasing δ^+, however, the Reynolds and viscous stress gradients rapidly dominate mean advection for $y^+ < y_m^+$, while mean advection remains the single largest term for $y^+ > y_m^+$ (figure 7*e,f*).

https://doi.org/10.1017/jfm.2011.253 Published online by Cambridge University Press

https://doi.org/10.1017/jfm.2011.253 Published online by Cambridge University Press

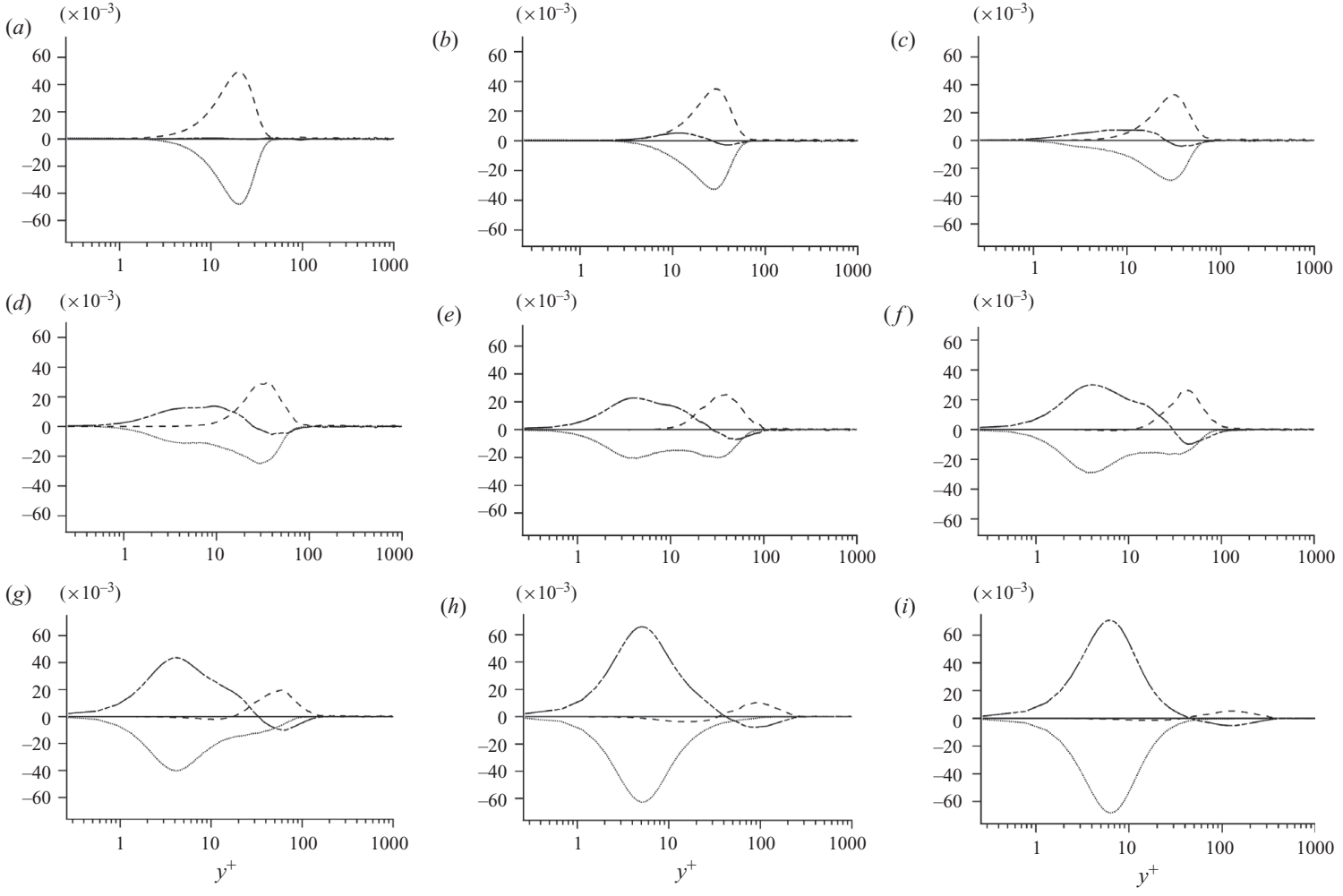


FIGURE 7. Evolution of the terms in (1.3) from the DNS of Wu & Moin (2009): · · ·, viscous stress gradient; - - -, mean advection; — - -, Reynolds stress gradient; (*a*) $\delta^+ = 35$, (*b*) $\delta^+ = 53$, (*c*) $\delta^+ = 58$, (*d*) $\delta^+ = 65$, (*e*) $\delta^+ = 76$, (*f*) $\delta^+ = 85$, (*g*) $\delta^+ = 111$, (*h*) $\delta^+ = 211$ and (*i*) $\delta^+ = 327$.

The former observation reveals a distinctly different formation process for layer II than in the channel flow. This largely stems from the fact that, at any given δ^+, the distribution of mean pressure gradient is constant across the channel. The latter observation is also distinct from channel flow and is consistent with the rapid growth of the boundary-layer thickness during transition. As the profile shapes proceed towards those characteristic of the four-layer regime (figure 7*g–i*), the non-zero portion of the mean advection profile is increasingly confined to y^+ values greater than the outer edge of layer II. Simultaneously, the non-zero portion of the viscous stress gradient is increasingly confined to y^+ values less than the inner edge of layer IV. For $\delta^+ \gtrsim 300$ the total mean inertia in layer II is almost entirely composed of the Reynolds stress gradient. On the other hand, layer IV forms owing to a diminishing mean viscous force, along with the gradient of the Reynolds stress forming an ever more exacting balance with mean advection. Early on and throughout the transitional regime, there is a region (nascent layer III) in which all three terms are of similar magnitude. This region is necessarily centred about y_m^+. Consideration of the stress gradient ratios below further clarifies how layer II comes into being quite differently from the channel flow. The ordering of terms characteristic of layer IV appears to develop well before layer II in the boundary layer. In the channel, however, layer IV develops prior to, but more closely in concert with, layer II. As δ^+ increases in the channel, the increasingly constant gradient associated with the increasingly linear layer IV Reynolds stress profile progressively develops to more closely balance the constant pressure gradient force. This is accomplished in concert with a concentration of the mean viscous stress gradient towards the surface. As indicated in figure 7, a qualitatively similar process also occurs in the boundary layer. In this case, however, the formation of an inertially dominated layer IV is characterized by two variable functions that attain balance as the viscous force diminishes. These results reveal that boundary-layer growth at high Reynolds number is almost exclusively affiliated with the action of the Reynolds stress gradient in layer IV.

The inner normalized amplitudes of the terms in figure 7(*a–i*) also undergo noteworthy developments. With the first appearance of a non-zero Reynolds-stress gradient profile, the amplitudes of the mean advection and viscous force terms exhibit a significant reduction (figure 7*b*, *c*), and the peak amplitudes of these profiles continue to decrease until $\delta^+ \simeq 75$. As δ^+ increases further, the balance between the viscous and Reynolds-stress gradient profiles for $y^+ < y_m^+$ is attained through the cancellation of increasingly larger magnitude functions (relative to inner scales), while the balance between the Reynolds stress gradient and mean advection for $y^+ > y_m^+$ is characterized by functions of diminishing peak amplitude. Over the same δ^+ range (approximately) the mean advection profile exhibits an interior zone of small but discernible negative excursion. At $\delta^+ = 327$ (figure 7*i*), the $-\partial\overline{uv}^+/\partial y^+$ profile attains its maximum value of about 0.07, with this maximum positioned near $y^+ = 6.5$. Existing evidence indicates that the magnitude of this near-wall peak varies little with further increases in Reynolds number, and that its position at large δ^+ is $y^+ \simeq 7$ (e.g. Klewicki 2010). The position of the outer (negative) peak in the $-\partial\overline{uv}^+/\partial y^+$ profile continuously moves outwards in y^+ units with increasing δ^+. The analysis of § 1.3 shows that this feature marks the upper end of an internal layer hierarchy upon which (1.3) realizes an increasingly self-similar form as $\delta^+ \to \infty$.

3.4.2. *Stress gradient ratios*

Figure 8 presents the ratio of the viscous stress gradient to Reynolds stress gradient, terms B/C in (1.3), versus y^+ for selected δ^+, $35 \lesssim \delta^+ \lesssim 370$. Thus, this plot has the

https://doi.org/10.1017/jfm.2011.253 Published online by Cambridge University Press

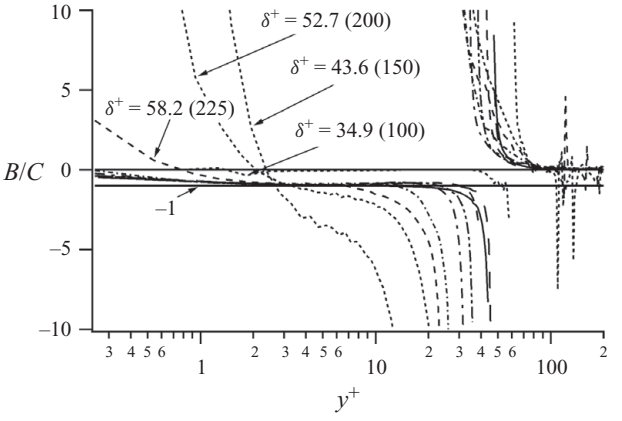


FIGURE 8. Ratio of the viscous stress gradient (term B) in (1.3) to the Reynolds stress gradient (term C) as a function of the Reynolds number from the boundary layer DNS of Wu & Moin (2009). Line styles are the same as in figures 2(*a*, *b*). Numbers in parentheses denote corresponding R_θ values.

same form as figure 1. The results in figure 8 are for the simulation of Wu & Moin (2009). All of the primary features of this plot are, however, closely mimicked by the DNS of Wu & Moin (2010), and, except for the one difference noted below, also correspond to those of the DNS by Wu (2010). An immediately discernible feature is the appearance of a layer III structure for all post-instability stage Reynolds numbers. This, of course, is the consequence of a non-zero peak in the Reynolds stress. Note also that the $\delta^+ \simeq 35$ profile only exhibits an excursion towards the -1 line, but does not cross this line as do all the other profiles. Elsnab *et al.* (2011) observed a similar behaviour in channel flow and described it as a localized patch of the mean effect of turbulent inertia embedded in a laminar-like background flow. As alluded to above, even by the remarkably low δ^+ of about 58, the ratio of figure 8 attains a value very close to the asymptotic value of -1 in a region $y^+ < y_m^+$. This signifies the onset of layer II formation shortly after layer III. The outward spread of layer II (in y^+ units) is also apparent, and is affiliated with the similar outward migration of y_m^+ quantified in figure 3. For $y^+ > y_m^+$, the lower δ^+ stress gradient ratios of figure 8 exhibit significantly non-zero values out to near $y^+ = \delta^+$. This reflects the persistence of a non-negligible mean viscous force.

The four-layer structure emerges differently in channels and boundary layers. These differences can be seen by comparing the results of figures 8 and 9. Owing to the constancy of the mean pressure gradient term in channel flow (at any given δ^+), the inward concentration of the mean viscous stress gradient occurs symmetrically with the outward spread of the Reynolds stress gradient (Elsnab *et al.* 2011). Because of this, the stress gradient ratio leading to the formation of layer II exclusively approaches -1 from below. For the simulations of Wu & Moin (2009, 2010) the -1 plateau is approached from above near the wall and from below farther from the wall but interior to y_m^+. This occurs in concert with the aforementioned process, by which the non-zero portion of the mean advection profile continually migrates outwards towards layer III with increasing δ^+ (see figure 7*a–i*). Conversely, the near-wall profiles from the passing wake simulation initially lie below the -1 line, but then pass through -1 and approach this asymptote from above as depicted in figure 8.

https://doi.org/10.1017/jfm.2011.253 Published online by Cambridge University Press

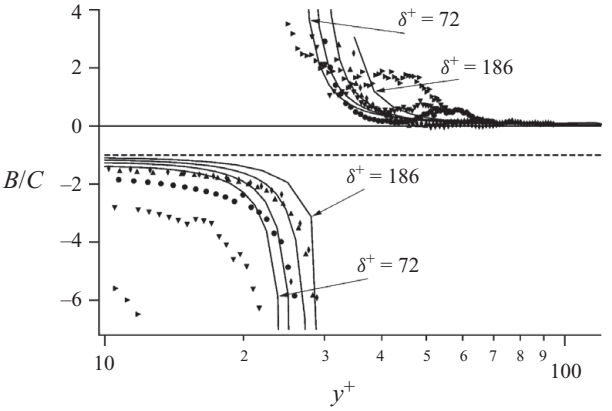


FIGURE 9. Ratio of the viscous stress gradient to the Reynolds stress gradient as a function of the Reynolds number for channel flow. Figure adapted from the study of Elsnab *et al.* (2011). Experimental data (solid symbols) range over $58 \leqslant \delta^+ \leqslant 98$, and DNS profiles (solid lines) range over $72 \leqslant \delta^+ \leqslant 186$.

Owing to the non-constancy of the mean advection profile, relatively complex processes mark the emergence of layer IV in the boundary layer. Elsnab *et al.* (2011) show that the process by which layer IV forms in channels includes the outward migration of a mean inertial zone. As in the boundary layer, this zone is characterized by the inflection point that marks the change from concave downward to concave upward curvature in the $-\overline{uv}^+$ profile. The channel flow analyses reveal that remnant viscous effects exist in a region outward of this inertial zone, and that these effects diminish and move to increasing y/δ with increasing δ^+. Evidence of the existence of a remnant mean viscous force region in boundary layers is also given in figure 8, but somewhat less distinctly than in the channel profiles of figure 9. During layer IV formation in channel flow, the Reynolds stress gradient increases to match the constant pressure gradient as the viscous stress gradient diminishes. Similarly, figure 7(*a–i*) shows that during layer IV formation in the boundary layer, the mean and turbulent inertia develop into equal and opposite but non-constant functions, as the viscous stress gradient diminishes. In the channel, the magnitude of the Reynolds stress gradient in layer IV apparently never exceeds the pressure gradient. In the zero-pressure gradient boundary layer, the layer IV Reynolds stress gradient never exceeds the magnitude of the mean advection.

3.4.3. *Minimum Reynolds number of the four-layer regime*

Figure 10 presents the inner normalized profiles of terms A, B and C at $\delta^+ \simeq 367$ along with the layer I–IV boundaries. The position of these boundaries is set in accord with the subjective, but self-consistent, criteria used by Wei *et al.* (2005*a*). The plot of figure 10 is deemed significant, since it represents the mean differential force balance for the minimum Reynolds number at which the ordering of terms in the mean momentum equation is estimated to first become representative of the high-Reynolds-number (four-layer) regime.

As in Elsnab *et al.* (2011), two primary criteria are used to determine this estimate. The first is that the much greater than ($\gg$) designation used to describe the ratio of terms in layers II and IV in figure 1 is satisfied by demanding that the smallest term has a magnitude less than 0.1 of the next smallest term when quantified near the centre of the respective layer. The second and related requirement is that the

https://doi.org/10.1017/jfm.2011.253 Published online by Cambridge University Press

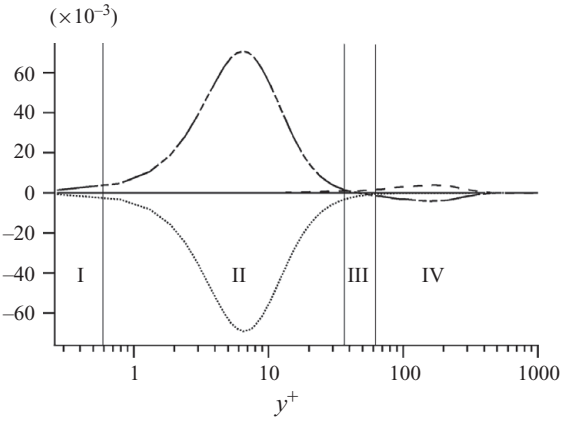


FIGURE 10. Profiles of the terms in (1.3) at the onset of the four-layer regime ($\delta^+ \simeq 367$, $R_\theta \simeq 780$): $\cdots$, viscous stress gradient; - - -, mean advection; — - -, Reynolds stress gradient. Data are from the simulation of Wu & Moin (2009). Vertical lines denote measured layer boundaries utilizing the criteria of Wei *et al.* (2005*a*).

layer thicknesses and the velocity increments across the layers are consistent with the scaling behaviours determined at much higher δ^+. As indicated by the entries in table 1, in the four-layer regime the Δy^+ thickness of layer II is close to $1.6\sqrt{\delta^+}$, while the layer II ΔU increment is close to $0.5U_\infty$. The stress gradient ratios of the present flows first satisfy the layer IV criterion at $\delta^+ \simeq 160$, where the magnitude of the Reynolds stress gradient first attains 10 times the magnitude of the viscous stress gradient near the centre of layer IV. On the other hand, while the ratio of terms B/C in figure 8 rapidly attains a value near -1 in layer II, the viscous stress gradient does not become 10 times the value of the mean advection term until $\delta^+ \simeq 330$. The layer width and scaling criteria do not develop to within about 5 % agreement of the high-Reynolds-number scalings until even greater δ^+. For example, for the layers depicted in figure 10 the inner normalized layer II thickness is measured to be $\Delta y^+_{II} \simeq 32.2$, while the scaling trend determined from higher Reynolds number data yields a value of $\Delta y^+_{\mathrm{II}} \simeq 30.7$. Similarly, the measured mean velocity increment across layer II for the profile of figure 10 is about $0.54U_\infty$. From these considerations, the four-layer regime is estimated to begin at $\delta^+ \simeq 360$ ($R_\theta \simeq 780$). As depicted in figure 4, this δ^+ closely coincides with the maximum value of C_f.

The application of the stated criteria to the data from the simulations of Wu & Moin (2010) and Wu (2010) yields qualitatively similar results. Some quantitative differences do, however, exist. These are associated with the δ^+ values at which the criteria associated with specific layers are first satisfied. The order in which the layers satisfy the criteria does not, however, change. For all of the present data, the overall onset of the four-layer regime corresponds closely with the Reynolds number at which C_f attains its maximum value.

To further test the sensitivity of these results to the method by which the flow was tripped to turbulence, the momentum balances associated with the spatially developing DNS of Schlatter & Orlu (2010) were also examined. Figure 11 depicts the terms in (1.3) for Reynolds numbers above and below that of figure 10. (Note that our calculations of δ^+ for the given R_θ are somewhat higher than the estimates made by Schlatter & Orlu 2010, and thus we also cite the R_θ values for more direct comparison.) As can be seen, both sets of profiles are highly similar. A closer

https://doi.org/10.1017/jfm.2011.253 Published online by Cambridge University Press

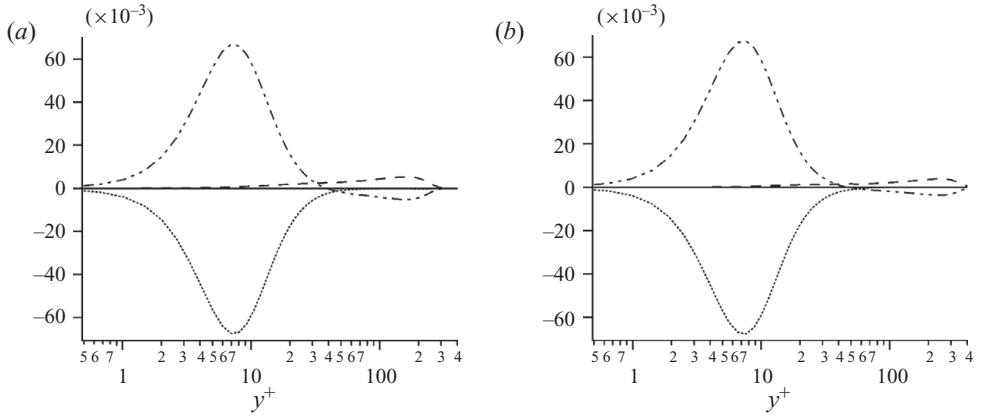


FIGURE 11. Profiles of the terms in (1.3) from the DNS of Schlatter & Orlu (2010): (*a*) $\delta^+ \simeq 251$ ($R_\theta = 670$) and (*b*) $\delta^+ \simeq 361$ ($R_\theta = 1000$). Line styles are the same as in figure 10.

examination, however, reveals that the mean advection term for their $R_\theta = 670$ profile retains significant magnitude into layer II, while examination of the associated stress gradient ratios (not shown) reveals a non-negligible viscous force near the outer edge of this flow. Thus, the profiles at this Reynolds number do not quite meet the stated criteria. By $R_\theta = 1000$, however, the criteria are met. Therefore, while there are some small differences, which are probably attributable to the method by which the flow was tripped, the results of figure 11 place the minimum R_θ of the four-layer regime between 670 and 1000, while the analysis of the data set of Wu & Moin (2009) puts it at $R_\theta \simeq 780$.

3.5. *Mean momentum field development*

An iconic trait of turbulent wall flows is a region of nearly logarithmic variation in the mean velocity profile. Existing evidence indicates that with increasing δ^+ this logarithmic variation becomes an increasingly better approximation over an increasingly larger y^+ domain, e.g. see data and discussion in Klewicki (2010). The mean profile is a solution to the boundary-value problem associated with (1.3). This fact, in concert with the above results relating to the onset of the four-layer regime, leads one to suspect that the dynamical mechanisms responsible for the emergence of logarithmic dependence are initiated relatively early on during the nonlinear development stage. This notion and related issues are now explored more deeply.

3.5.1. *Emergence of logarithmic behaviour*

The so-called indicator function, $\Xi = y^+ \partial U^+ / \partial y^+$, is often employed to explore questions pertaining to logarithmic dependence. In a region of (nearly) logarithmic variation, this function will attain a (nearly) constant value equalling the leading coefficient of the logarithmic equation. Of course, the inverse of this leading coefficient is typically called the von Kármán constant (coefficient), κ. Figure 12 presents Ξ profiles in the range $35 \lesssim \delta^+ \lesssim 370$. These data show that the evolution of Ξ is characterized by an internal peak that broadens and diminishes in amplitude. This internal peak flattens into a dual peak structure, with the zone between the two peaks continuing to attenuate, eventually reflecting the emergence of approximately logarithmic dependence. This sequence is consistent with the experimental measurements of Ching *et al.* (1995) for $400 \lesssim R_\theta \lesssim 1320$. Regarding

https://doi.org/10.1017/jfm.2011.253 Published online by Cambridge University Press

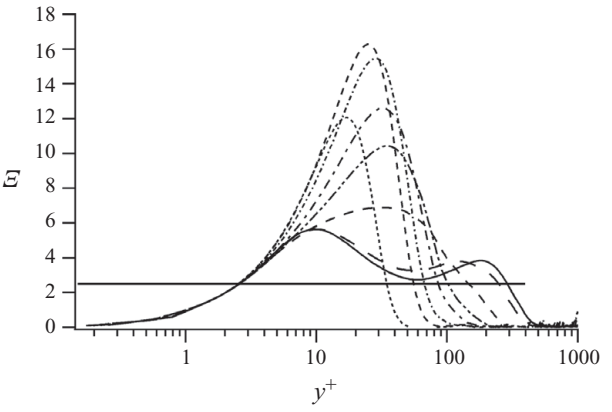


FIGURE 12. Profiles of the function $\Xi = y^+ \partial U^+/\partial y^+$ for varying δ^+. Data are from the simulation of Wu & Moin (2009). Line styles correspond to those given in figure 2.

the later discussion of the lower extent of the L_β hierarchy, it is also noteworthy that Ching *et al.* (1995) observed a Reynolds number effect on Ξ down to about $y^+ = 8$.

A comparison with figures 7(*a–i*), 8 and 10 indicates that Ξ does not begin to exhibit the eventual form just described until the *balance breaking and exchange* of mean forces across layer III becomes distinct. Mean dynamics representative of the high δ^+ ordering of terms in (1.3) were estimated to first exist for $\delta^+ \gtrsim 360$ ($R_\theta \gtrsim 780$). It is thus worth noting that at essentially the same δ^+ value, Ξ first approaches the $1/\kappa$ line at a point of tangency. Higher-Reynolds-number data reveal that, for a range of y^+ values greater than this initial point of tangency, Ξ develops a plateau-like region that grows in inner normalized width and increasingly approximates constancy as $\delta^+ \to \infty$ (Nagib & Chauhan 2008). Elsnab *et al.* (2011) provide rather clear evidence that the evolution towards a plateau-like zone in the Ξ profile occurs similarly but somewhat differently in the channel. The differences are related to the differing rates at which Ω_z concentrates nearer to the surface (see figure 6), and is also connected to the evolution of the mean advection term (figure 7*a–i*), for which there is no analogous process in the channel.

A number of observations can also be made that, within the context of the theory presented in § 1.3, pertain to the manner by which (1.3) and its approximation (1.5) first begin to admit an approximately logarithmic mean profile solution. One is that the region of negative curvature in the $T^+ = -\overline{uv}^+$ profile (beginning interior to y_m^+ and extending beyond y_m^+) is established early in the nonlinear development stage. This observation is similar to that seen in channel flow (Elsnab *et al.* 2011). The $-\partial\overline{uv}^+/\partial y^+$ profiles subsequently undergo a complex evolution (figure 7*d–g*) that is distinct from channel flow. Over this δ^+ range, the non-zero portion of the mean advection profile migrates outwards. Once this occurs, the $-\partial\overline{uv}^+/\partial y^+$ profiles attain a shape qualitatively similar to that in the four-layer regime (figure 7*h*). From these observations, we surmise that, prior to the establishment of the four-layer regime, the mechanism of turbulent inertia rearranges both the mean viscous force and mean advection profiles, with the former concentrating near the surface (nascent layer II), and the latter concentrating near the free stream (nascent layer IV). Conversely, in the channel, turbulent inertia only redistributes the mean viscous force. These observations are consistent with the more rapid wallward concentration of mean vorticity in the channel (figure 6), and the fact that the channel flow $-\mathrm{d}\overline{uv}^+/\mathrm{d}y^+$

https://doi.org/10.1017/jfm.2011.253 Published online by Cambridge University Press

profile establishes a shape that is qualitatively similar to that in the four-layer regime essentially from the onset of the nonlinear development stage (Elsnab *et al.* 2011).

In both the channel and the boundary layer, the theory outlined in § 1.3 identifies the establishment of the balance breaking and exchange of terms across layer III (and the underlying self-similar structure of the L_β hierarchy) as an essential prerequisite for the emergence of a logarithmic mean profile. The supporting observational evidence is provided by noting that the only profiles in figure 2(*a*) that can rationally be said to have an emerging logarithmic region are at $\delta^+ \simeq 327$ and 367 (also see figure 12). Consistently, the mean momentum balance data represented in figures 7(*i*) and 10 are the first to approximate the ordering of terms associated with the four-layer regime – a central attribute of which is the distinct balance breaking and exchange of forces across layer III.

3.5.2. *Emergence of the L_β scaling layer hierarchy*

Although useful for identifying logarithmic-like behaviours, Ξ has no analytical connection to (1.3). Thus, it is desirable to pursue more theoretically well-founded evidence. In the context of the theory described in § 1.3, such evidence includes an approximately and increasingly constant value of $A(\beta)$ on the hierarchy (as $\delta^+ \to \infty$), or equivalently, an approximately and increasingly linear $W(y^+)$ distribution on the hierarchy. These attributes were explicitly demonstrated for transitional channel flow by Elsnab *et al.* (2011). For channel flow, the application of the theory is simpler since the pressure gradient is a constant function of y having a simple dependence on δ^+. Neither of these mathematically attractive features holds for the analogous mean advection profile in the boundary layer. As noted in § 1.3, however, important similarities exist between the mathematical structure of the boundary layer and channel flow equations. In either case, the relevant order of magnitude estimate indicates that

$$W(y^+) = O(\beta^{-1/2}). \tag{3.2}$$

For the channel, β is evaluated using

$$\beta = \frac{\mathrm{d}T^+}{\mathrm{d}y^+} + \epsilon^2 = -\frac{\mathrm{d}^2U^+}{\mathrm{d}y^{+2}}. \tag{3.3}$$

In this case $\epsilon^2 = 1/\delta^+$, with the last equality in (3.3) directly following from the channel flow mean momentum equation. Within the approximation of (1.5), one can similarly estimate $W(y^+)$ for the boundary layer. In this case, it is reasonable to expect that the qualitative features of the $W(y^+)$ profile will be preserved, but the slope of the $W(y^+)$ profile may not provide a precise estimate for κ, especially at low δ^+.

The $W(y^+)$ profiles of figure 13 support these expectations. Specifically, the $\delta^+ \simeq 327$ and 367 profiles provide evidence of an emerging linear portion in the $W(y^+)$ profile. Furthermore, relative to the theory, as well as previous observations in channels, pipes and boundary layers (Osterlund *et al.* 2000; Nagib & Chauhan 2008; Klewicki *et al.* 2009; Elsnab *et al.* 2011), it is anticipated that logarithmic behaviour will be approached most rapidly on an internal sub-domain of the hierarchy where the dominant terms in (1.3) are inertial. This corresponds to a sub-domain starting near the outer edge of layer III and ending interior to the upper limit of the hierarchy, denoted by the position where W is maximal. According to both the theory and observations, the outer edge of layer III is located at $y^+ \simeq 2.6\sqrt{\delta^+}$ (see table 1). For the $\delta^+ = 367$ profile of figure 13, layer III ends at $y^+ \simeq 50$, while the position of W_{max} is $y^+ \simeq 165$. Fife *et al.* (2009) analytically estimate that the maximal position of the

https://doi.org/10.1017/jfm.2011.253 Published online by Cambridge University Press

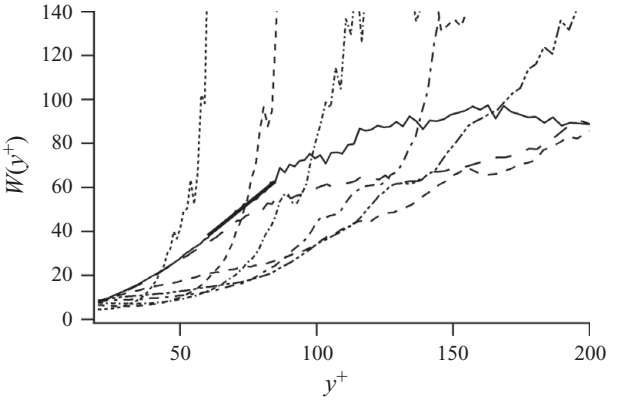


FIGURE 13. Estimates of the length-scale width distribution for the boundary layer L_β hierarchy as a function of δ^+. Data are from the simulation of Wu & Moin (2009). Line styles are the same as those used in figure 2. The curve fit (thick black line) is given by $W = 1.015y^+ - 23.27$.

hierarchy is $O(\delta)$, and for channel flow is located near $y/\delta = 0.5$. The $W(y^+)$ profile of figure 13 places it at $y/\delta \simeq 0.45$. Klewicki *et al.* (2009) found that W_{max} is also located at $y/\delta \simeq 0.45$ in four-layer regime channel flows. Over the domain $52 \lesssim y^+ \lesssim 85$, the $\delta^+ = 367$ profile is convincingly fit by the linear equation, $W = 1.015y^+ - 23.27$, with an R-factor of 0.99, and ± 1 standard deviation uncertainties in the slope and intercept of 0.015 and 1.04, respectively. Examination of the $W(y^+)$ data of Wu & Moin (2010) and Wu (2010) reveals that the features of the $\delta^+ = 367$ profile of figure 13 are preserved at higher δ^+. For example, these profiles reveal an increasing linear region located between the outer edge of layer III and the position of W_{max}, and that in all cases W_{max} is located at $y/\delta \simeq 0.45$. There is also some indication that the slope of the linear region in the estimated $W(y^+)$ profile decreases with increasing δ^+.

This last observation may have connection to some noteworthy differences between the $W(y^+)$ profiles in channels and boundary layers. For comparison, the channel flow results of Elsnab *et al.* (2011) are plotted in figure 14. Qualitatively, once in the sub-domain of linear dependence, the channel flow $W(y^+)$ profile remains essentially linear up to the wall-normal position of its maximal value, W_{max}. This is clearly not the case for the $\delta^+ = 367$ profile of figure 13, although, as just noted, there may be a trend towards this condition as δ^+ increases. In fact, the results of figure 15 from the higher-Reynolds-number data of Schlatter & Orlu (2010) support this hypothesis, as the slope of the linear region clearly shows a decreasing trend with increasing δ^+. It is therefore relevant to note that in channel flow the actual $W(y^+)$ distribution is much more well approximated by a straight line between W_{min} and W_{max} (see figure 14), and that for the channel Klewicki *et al.* (2009) showed that $W(y^+)$ is not only linear, but that for a range of y^+ values starting near the outer edge of layer III $\mathrm{d}W/\mathrm{d}y^+ = \sqrt{\kappa}$. A straight line drawn between W_{min} and W_{max} in figure 13 has a slope of about 0.6. Interestingly, $\mathrm{d}W/\mathrm{d}y^+ = 0.6$ corresponds to $\kappa \simeq 0.36$; a profile slope nearly identical to that observed in figure 2. Thus, these observations lend support to the hypothesis that the linear region of the $W(y^+)$ profile corresponds to logarithmic-like behaviour at essentially all δ^+ in the four-layer regime, but that the slope of this profile only allows the accurate estimation of κ as $\delta^+ \to \infty$. In the channel, however, both of these attributes associated with $W(y^+)$ apparently emerge simultaneously. Quantitatively, a value of $W_{max} \simeq 0.33\delta^+$ is established as early as $\delta^+ = 90$ in transitional channel

https://doi.org/10.1017/jfm.2011.253 Published online by Cambridge University Press

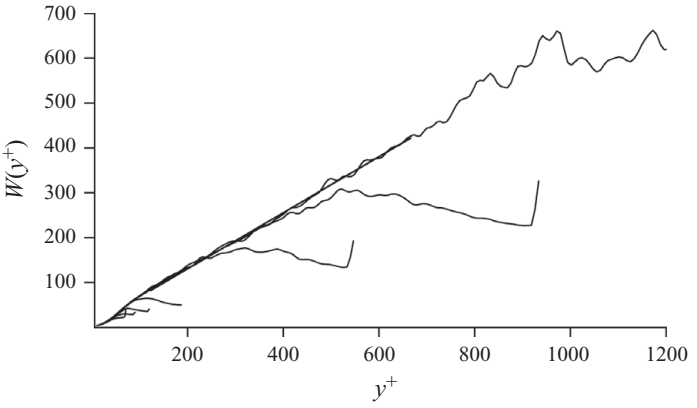


FIGURE 14. Inner normalized characteristic lengths associated with the continuous hierarchy of scaling layers admitted by the momentum equation for turbulent channel flow (Fife *et al.* 2005*b*). Data are from the DNS studies of Laadhari (2002) at $\delta^+ = 72, 90$ and 120, and Hoyas & Jimenez (2006) at $\delta^+ = 186, 547, 934$ and 2004. The curve fit of the $\delta^+ = 2004$ profile yields $W = 0.6247y^+ + 5.61$ for $118 \leqslant y^+ \leqslant 667$, see Klewicki *et al.* (2009). Adapted from Elsnab *et al.* (2011).

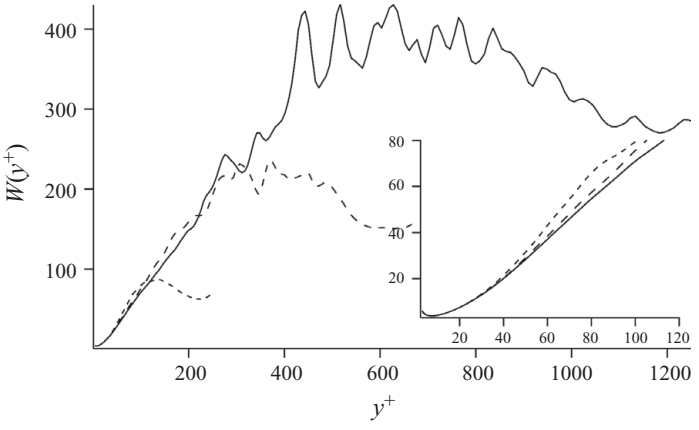


FIGURE 15. $W(y^+)$ distributions from the boundary-layer DNS of Schlatter & Orlu (2010): – – –, $\delta^+ = 251$; — —, $\delta^+ = 671$; ——, $\delta^+ = 1245$.

flow, which is consistently maintained up to at least $\delta^+ = 2004$ (Elsnab *et al.* 2011). The value of W_{max} in figure 13 is approximately $0.27\delta^+$, while those in figure 15 are estimated to range between 0.28 and 0.32.

3.5.3. *The evolution of turbulent inertia*

The properties of $W(y^+)$ are relevant only when evaluated on the L_β hierarchy, where they fundamentally depend on the decay rate of $\partial T^+/\partial y^+ = -\partial \overline{uv}^+/\partial y^+$ (Fife *et al.* 2009). To clarify how the features of this profile develop with increasing δ^+, in figure 16(a,b) we replot the $\partial T^+/\partial y^+$ profiles of figure 7$(a$–$i)$ relative to the outer and inner normalized distance from the wall, respectively. Important properties of the mean dynamics are affiliated with the positions and amplitudes of the positive and negative peak values in these profiles. The positive peak interior to y_m^+ is associated with the change from concave upward to concave downward curvature in the $-\overline{uv}^+$ profile, and the negative peak exterior to y_m^+ is associated with a change in curvature

https://doi.org/10.1017/jfm.2011.253 Published online by Cambridge University Press

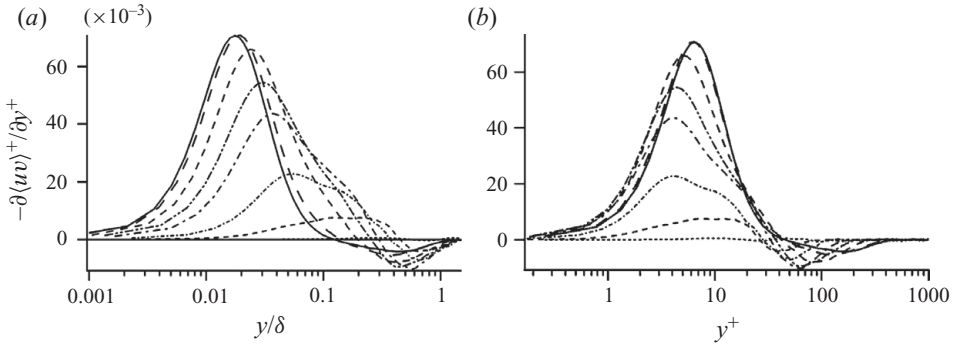


FIGURE 16. Profiles of $-\partial\overline{uv}^+/\partial y^+$, term C in (1.3) for varying δ^+: (a) plotted versus y/δ and (b) plotted versus y^+. Data are from the simulation of Wu & Moin (2009). Line styles are the same as given in figure 2.

from concave downward to concave upward. (Recall that the maxima in $-\partial\overline{uv}^+/\partial y^+$ are the inflection points in $-\overline{uv}^+$, and that y_m^+ corresponds to the zero crossing of $\partial T^+/\partial y^+$.) As discussed relative to figure 7(a–i), by $\delta^+ \simeq 367$ the positive (momentum source-like) peak has settled into a y^+ position and magnitude that varies little with further increases in δ^+. This is shown in figure 16(b). On the other hand, the negative (momentum sink-like) peak continually changes amplitude and y^+ position. As revealed in figure 16(a), both peaks and the zero crossing of the Reynolds stress gradient initially move inwards under outer normalization. With the advent of the four-layer regime, however, the outer peak settles into a fixed y/δ value (see below), while the zero crossing and inner peak continue to move to smaller y/δ values, albeit at different rates.

Given the increasingly invariant inner normalized properties of the near-wall peak, the reduction in the outer peak amplitude in figure 16(b) must occur in concert with its outward migration in y^+. This is true since

$$\int_0^{\delta^+} \partial T^+/\partial y^+ \,\mathrm{d}y^+ = 0. \tag{3.4}$$

Figure 17 shows this and other features by plotting the pre-multiplied Reynolds stress gradient versus the length scale intrinsic to layers II and III. Pre-multiplication reveals the equal areas of the positive and negative contributions on a logarithmic graph. Under the $y/\sqrt{\nu\delta/u_\tau}$ ($\equiv y^+/\sqrt{\delta^+}$) normalization, the zero crossing settles into a fixed position, and, with increasing δ^+, the inner and outer peaks move away from this point in a manner that satisfies the integral constraint. In the context of the theory described in § 1.3, this reflects the growth of the L_β hierarchy. The outward migration of the negative peak is commensurate with the emerging self-similarity between the rates at which the first and second derivatives of the Reynolds stress decay with increasing y^+. This is seen more clearly by examining (1.13) and recognizing that β depends on the decay rate of $\partial T^+/\partial y^+$. In the channel, this self-similarity is more perfectly realized as the $\epsilon^2 = 1/\delta^+$ term in (3.3) becomes small. In the boundary layer, this self-similarity is more perfectly realized as the corresponding $\epsilon^2 b$ term in (1.5) becomes small – recall that in this case $\epsilon^{-2} = O(\delta^+)$ and $b = O(1)$.

Connections exist between figures 13 and 16(b). For example, the wall-normal range over which $W(y^+)$ most rapidly approximates linearity corresponds to a region starting slightly beyond the zero crossing of the $\delta^+ = 367$ $\partial T^+/\partial y^+$ profile, but ending

https://doi.org/10.1017/jfm.2011.253 Published online by Cambridge University Press

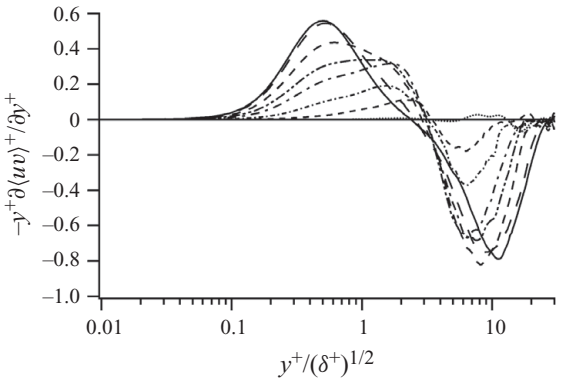


FIGURE 17. Profiles of $-y^+\partial\overline{uv}^+/\partial y^+$, pre-multiplied term C in (1.3) for varying δ^+, and plotted versus $y/\sqrt{\nu\delta/u_\tau} = y^+/\sqrt{\delta^+}$. Data are from the simulation of Wu & Moin (2009). Line styles are the same as given in figure 2.

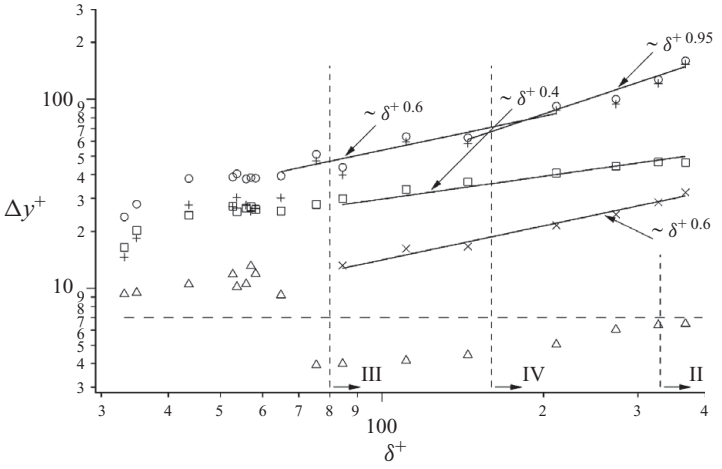


FIGURE 18. Inner normalized wall-normal positions and relative positions of the inner and outer peaks of $-\partial\overline{uv}^+/\partial y^+$ plotted versus δ^+: △, inner (positive) y^+ peak positions ($y^+_{p_i}$); ○, outer (negative) y^+ peak positions ($y^+_{p_o}$); +, $\Delta y^+_p = y^+_{p_o} - y^+_{p_i}$; □, y^+_m = positions of the zero crossings of $-\partial\overline{uv}^+/\partial y^+$; ×, $\sqrt{y^+_{p_i} y^+_{p_o}}$; – – –, $y^+ = 7$.

significantly interior to its negative peak. That is, the outer peak in $\partial T^+/\partial y^+$ (inflection in $-\overline{uv}^+$) also provides an estimate for the upper limit of the L_β hierarchy. This is made explicit by (1.12) and (1.13), demonstrating that $A(\beta)$ changes sign at this point. Consistent with the theory, the $\delta^+ = 367$ profile of figure 16(*a*) attains its outer peak at $y^+ \simeq 165$, as does the corresponding position of W_{max}.

The trends associated with the positions of the positive and negative peaks depicted in figures 16 and 17 also describe how the inner and outer lengths become relevant to the scaling properties of the four-layer regime. Figure 18 plots the positions of the inner and outer peaks, as well as the Δy^+ distances between these peaks for $35 \lesssim \delta^+ \lesssim 370$. For reference, the positions of the zero crossings, y^+_m, from the simulation of Wu & Moin (2009) are also repeated from figure 3. The features now described are also reflected in the data from the other simulations.

https://doi.org/10.1017/jfm.2011.253 Published online by Cambridge University Press

The near-wall peak in $-\partial\overline{uv}^+/\partial y^+$ moves slightly outwards (from $y^+ \simeq 9$ to $y^+ \simeq 12$) for increasing δ^+, but for $\delta^+ \lesssim 60$. Recall that this is slightly above the critical value, $\delta^+ \simeq 50$. Between $\delta^+ \simeq 60$ and 75, however, this inner peak abruptly moves to $y^+ < 4$. Figure 3 shows that the peaks in the Reynolds stress distribution move outwards rapidly for subcritical flows subject to finite three-dimensional perturbations. Between $50 \lesssim \delta^+ \lesssim 60$, the $-\overline{uv}^+$ profile is spatially localized, but is both broadening and increasing in peak amplitude. Relative to transitional channel flow, Elsnab *et al.* (2011) associate these processes with the spreading of the Reynolds stress gradient towards the boundaries. The dramatic wallward progression for $60 \lesssim \delta^+ \lesssim 75$ is taken to mark the robust onset of the nonlinear development stage. (The coincidence between when this occurs and when the Reynolds stress gradient becomes non-zero in the immediate vicinity of the wall leads one to suspect that this marks the onset of the so-called near-wall cycle, e.g. see Schoppa & Hussain 2002; Waleffe 1997.) Once operative, nonlinear interactions are expected to rapidly enhance the transport of streamwise momentum towards the surface. Owing to the no-slip condition, both the slope and curvature of the mean momentum profile are expected to significantly amplify. These expectations are verified by figures 4 and 7(*c–e*). Between $75 \lesssim \delta^+ \lesssim 330$, the amplitude of the inner peak increases by a factor of about 2.5, yet the inner peak only moves outwards to $y^+ \simeq 6.5$. All existing evidence indicates that for $\delta^+ \gtrsim 330$ the position of the inner peak remains nearly fixed, settling into its high δ^+ position of $y^+ \simeq 7$. As found in § 3.4.3, the effects of mean advection do not become negligible in the emergent layer II until $\delta^+ \simeq 330$. In the context of the theory, the near-wall *anchoring* of the inner peak in the Reynolds-stress gradient profile (at $y^+ = y^+_{p_i}$) marks the point at which ν/u_τ characterizes the smallest dynamically relevant turbulence length scale, i.e. when the inner length first becomes a scaling parameter relevant to connecting different δ^+ flows within the four-layer regime.

A comparison of the outer peak and zero-crossing data of figure 18 reveals that for $\delta^+ \lesssim 60$ the two positions track each other, while for $\delta^+ \gtrsim 60$ they diverge. Between $60 \lesssim \delta^+ \lesssim 160$, the rate of divergence is greater than $\sim\sqrt{\delta^+}$, but less than $\sim\delta^+$. Physically, the reason for this is the persistence of a non-negligible mean viscous force in the outer region (see figure 8). Thus, although this is demonstrated by a curve fit having a single slope, the actual power law continuously varies between something greater than $\delta^{+1/2}$ and something approaching δ^{+1}. The mean viscous stress gradient was determined in § 3.4.3 to become less than 1/10 of the Reynolds stress gradient in the emergent layer IV at $\delta^+ \simeq 160$. As evidenced by the curve fit using the $\delta^+ > 150$ data, once this occurs the outer peak begins to move outwards at a rate approximately proportional to δ^+. In the context of the theory, the *anchoring* of the outer Reynolds-stress gradient peak position (denoted by $y^+_{p_o}$) as a constant fraction of δ^+ marks the point at which δ characterizes the largest dynamically relevant turbulence length scale, i.e. when the outer length first becomes a scaling parameter relevant to connecting different δ^+ flows within the four-layer regime.

The $\Delta y^+_p = y^+_{p_o} - y^+_{p_i}$ profile similarly tracks the y^+_m profile for $\delta^+ \lesssim 60$. The fact that the Δy^+_p profile very nearly falls on top of the y^+_m profile for $\delta^+ \lesssim 60$ is evidence that the $-\overline{uv}^+$ profile is at first symmetrically distributed about its maximum value. For $\delta^+ \gtrsim 60$, however, strong asymmetries develop. Following its abrupt shift towards the wall, $y^+_{p_i}$ migrates towards an essentially fixed inner normalized position. Thus, for greater δ^+, Δy^+_p is effectively dictated by the variation in $y^+_{p_o}$.

Figure 18 shows layer III starting at $\delta^+ \simeq 80$, or equivalently, shortly after the onset of the nonlinear development stage. Consistently, the curve fit of the $\delta^+ > 80$ $-\overline{uv}^+$ data reveals a power law for y^+_m close to, but slightly less than, $\sqrt{\delta^+}$ ($\sim\delta^{+0.4}$). This

https://doi.org/10.1017/jfm.2011.253 Published online by Cambridge University Press

is broadly consistent with previous observations at low δ^+ (e.g. see the data review in Buschmann, Indinger & Gad-el-Hak 2009). As noted above, for $\delta^+ \lesssim 160$, the mean viscous force remains significant in the emergent layer IV, while for $\delta^+ \lesssim 330$ mean advection is still significant in the emergent layer II. As the influences of mean advection and the mean viscous force respectively diminish in layers II and IV, the inner and outer lengths increasingly gain definition as the bounding length scales of the L_β hierarchy. As discussed relative to figures 7 and 8, this occurs owing to the action of turbulent inertia as increasingly constrained by the boundary conditions. We thus surmise that even when layer III is not bounded from above by a fully inertial layer IV or from below by a layer II solely comprised of a stress gradient balance layer, y_m^+ still exhibits a dependence close to $\sqrt{\delta^+}$.

3.5.4. *Estimating* λ

Once the four-layer structure comes into being, the behaviour of y_m^+ apparently becomes estimable in terms of L_β hierarchy properties. Two similar interpretations are operative. One relates to upper and lower bounds of the hierarchy sub-domain, while the other relates to the bounds of the $W(y^+)$ distribution that resides on the hierarchy. In the $\delta^+ \to \infty$ limit of a perfectly self-similar hierarchy, these two interpretations are expected to become equivalent.

The first interpretation identifies y_m^+ as the centre position of a linear hierarchy on a domain whose end points, $y_{p_i}^+$ and $y_{p_o}^+$, are moving apart according to $\Delta y_p^+ \sim \delta^+$, see figure 18. On one side of y_m^+ the Reynolds stress gradient acts like a momentum source and (1.3) is satisfied by a balance between the Reynolds and viscous stress gradients. On the other side of y_m^+, it acts like a momentum sink and the dominant terms are both inertial. The centre position of such a hierarchy is simply given by its geometric mean, i.e.

$$y_m^+ = \sqrt{y_{p_i}^+ y_{p_o}^+}. \tag{3.5}$$

The efficacy of this expression is explored in figure 18 by plotting $\sqrt{y_{p_i}^+ y_{p_o}^+}$ versus δ^+. These data clearly indicate that (3.5) becomes increasingly accurate with the emergence of the four-layer regime. Perhaps more significantly, the asymptotic estimates of $y_{p_i}^+ \simeq 7$ and $y_{p_o}^+ \simeq 0.5\delta^+$ (based upon channel flow analysis) provide an explicit prediction for λ at large δ^+,

$$y_m^+ = \sqrt{y_{p_i}^+ y_{p_o}^+} = \sqrt{3.5\delta^+} = 1.87\sqrt{\delta^+}. \tag{3.6}$$

Remarkably, the indicated coefficient is identical to that first measured by Long & Chen (1981). Similarly, if the measured value for $y_{p_o}^+ \simeq 0.45\delta^+$ is employed then $\lambda = 1.77$. Lastly, the use of the $R_\theta = 3970$ ($\delta^+ = 1245$) boundary-layer data of Schlatter & Orlu (2010) in (3.5) yields a larger value for λ of 2.28. This larger value is primarily because $y_{p_o}^+ = 0.707$, although $y_{p_i}^+$ is also larger at 7.36. It is, however, potentially significant to note that the use of $\lambda = 2.28$ yields an estimate for y_m^+ of 80.4, whereas the actual Reynolds stress profile self-consistently peaks between $78.0 \leqslant y_m^+ \leqslant 81.2$. This essentially exact prediction leads one to suspect that the outer edge of the L_β hierarchy in the boundary layer, while adhering to (3.5) and always remaining $O(\delta)$, may attain a larger asymptotic y/δ value than in the channel. Relative to the theory, this most probably relates to the fact that the details of the mean advection profile shape function, b, are not *a priori* known (see § 1.3).

The second interpretation identifies y_m^+ as residing within the *central* width of the linear $W(y^+)$ distribution, which, as indicated in table 1, is predicted to have the width of layer III, W_{III}. This width is estimated by the geometric mean of W_{min} and

https://doi.org/10.1017/jfm.2011.253 Published online by Cambridge University Press

W_{max} on the hierarchy,

$$W_{\mathrm{III}} = \sqrt{W_{min} W_{max}}. \tag{3.7}$$

Inserting the values of $W_{min} \simeq 4$ (at $y_{pi}^{+} = 7$) and $W_{max} \simeq 0.27\delta^{+}$ (at $y/\delta \simeq 0.45$) from the $\delta^{+} = 367$ profile of figure 13 into (3.7) gives $W_{\mathrm{III}} \simeq 1.04\sqrt{\delta^{+}}$. This is compared to the independently estimated width of layer III of about $1.0\sqrt{\delta^{+}}$ that, according to the theory, is a member of the L_{β} hierarchy centred about y_{m}^{+}. The veracity of this estimate reinforces the previous assertion that layer III (centred about y_{m}^{+}) constitutes the mean member of the hierarchy.

4. Discussion and conclusions

Interpretations were primarily embedded within the data presentation. Thus, in this section we provide a brief summary of the broader physical and theoretical implications of the present study.

4.1. *Physical implications*

The present evidence supports the assertion that the mechanism of turbulent inertia, as reflected in the mean by the Reynolds stress gradient, drives flow field evolution through the transitional regime. A similar conclusion was reported by Elsnab *et al.* (2011) for channel flow. In the boundary layer, however, the Reynolds stress gradient rearranges both the viscous stress gradient and mean advection profiles prior to the establishment of the four-layer regime. This is distinct from the channel where the pressure gradient is always a constant function, and only the mean viscous stress gradient undergoes qualitative rearrangement. This distinction underlies a number of differences, as noted throughout. These include that the transitional regime occurs over a significantly larger δ^{+} range in the boundary layer. Similarly, the four-layer regime in the present boundary layers begins close to where the C_f versus R_θ curve peaks. Whether this continues to hold for all types of initiating instabilities remains to be fully explored. That is, while the data of Schlatter & Orlu (2010) in figures 6 and 11(a,b) closely adhere to the data of Wu & Moin (2009, 2010) and Wu (2010), the peak in the C_f curve associated with the DNS of Schlatter & Orlu (2010) occurs nearer to $R_\theta = 400$. In contrast, the C_f curves in figure 4 all peak near $R_\theta = 780$. In the channel, the difference is unambiguous, as the onset of the four-layer regime occurs at a δ^{+} value significantly greater than the δ^{+} of this peak (see figure 5).

Figure 19 provides a depiction of the evolving dynamical mechanisms through transition. As discussed relative to figures 7 and 8, the process nominally begins with the first appearance of a finite Reynolds stress distribution, and the concomitant juxtaposition of positive and negative Reynolds stress gradients. Relative to the four-layer regime, Klewicki *et al.* (2007) describe these adjacent momentum source and sink mechanisms in connection with the simultaneous processes underlying wallward momentum transport and the outward transport of Ω_z associated with boundary-layer growth. In the transitional regime, these mechanisms are responsible for the segregation of forces leading to the four-layer ordering of terms. As described in §§ 3.4.3 and 3.5.3, with increasing δ^{+} the layers of figure 1 emerge in the following order: layer III ($\delta^{+} \simeq 80$), layer IV ($\delta^{+} \simeq 160$), and layers II and I ($\delta^{+} \simeq 330$), with the δ^{+} values in parentheses derived from the simulation of Wu & Moin (2009). The last two δ^{+} values mark the points at which δ and ν/u_τ become parameters relevant to scaling the mean dynamics in the four-layer regime. In the other simulations the layers form in the same order and are realized at nearly the same δ^{+}. As depicted in figure 19,

https://doi.org/10.1017/jfm.2011.253 Published online by Cambridge University Press

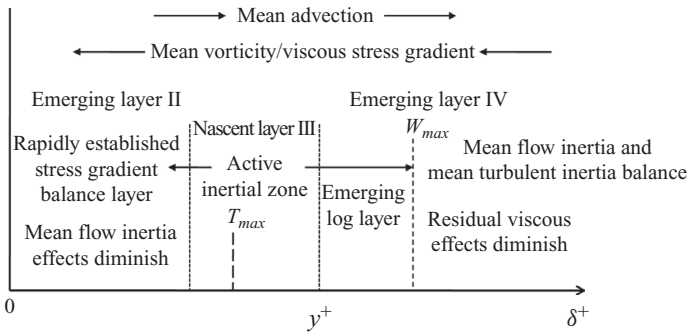


FIGURE 19. Schematic representation of the momentum and vorticity redistribution processes during transition that eventually lead to the four-layer structure characteristic of high-Reynolds-number flow, see figure 1. The arrows denote the relative expansion of the noted regions/influences when viewed from a vantage point fixed on y_m.

the evolution towards the four-layer structure involves the inward concentration of mean viscous stress gradient and the outward concentration of mean advection.

The L_β hierarchy is formally admitted by the mean dynamical equation. Its formation is marked by the emergence of a distinct balance breaking and exchange of forces across layer III. Physically, it exists owing to a state of self-similar mean dynamics (approximate at any finite Reynolds number) that is replicated across a range of scales and over an interior domain having precisely estimable upper and lower boundaries. The widths of the hierarchy layers asymptotically scale with distance from the wall. For this and other reasons, there are striking similarities between its representation of mean dynamics and the hairpin vortex/attached eddy paradigm of wall turbulence (e.g. see Townsend 1976; Perry & Chong 1982; Perry & Marusic 1995; Adrian 2007; Klewicki 2010; Smits, McKeon & Marusic 2011, and references therein). Together with the visualization results from the simulations employed herein (also see Marusic 2009), the present analysis regarding the origin and emergence of the four-layer regime provides evidence that this paradigm becomes operative shortly after the initiation of the nonlinear development stage ($\delta^+ \gtrsim 70$), and that the mean dynamical flow properties at much higher δ^+ have a clear connection to these early non-laminar flows.

In affiliation with this, there are a number of observations of wall-flow structure having potential connection to the properties of the L_β hierarchy. For example, the study of Tomkins & Adrian (2003) provides evidence of the linear spanwise scale growth with distance from the wall. Similarly, the larger maximal value of $W(y^+)/\delta^+$ in channel flow relative to boundary-layer flow has intriguing correlation with observations of discernible differences in the larger-scale motions within these flows (e.g. see Monty *et al.* 2007; Balakumar & Adrian 2007; Bailey *et al.* 2008). Given these observations, it is also rational to speculate that the differences between the rates at which a linear $W(y^+)$ distribution forms in channels in boundary layers are connected to small but discernible variations in the manner by which the layer IV motions, as constrained by the boundary conditions (and especially those of the vorticity field), develop with increasing δ^+.

4.2. *Theoretical implications*

Through transitional flow, the onset of nonlinear interactions results in a rapid amplification and broadening of the $-\partial\overline{uv}^+/\partial y^+$ profile. Within the nonlinear

https://doi.org/10.1017/jfm.2011.253 Published online by Cambridge University Press

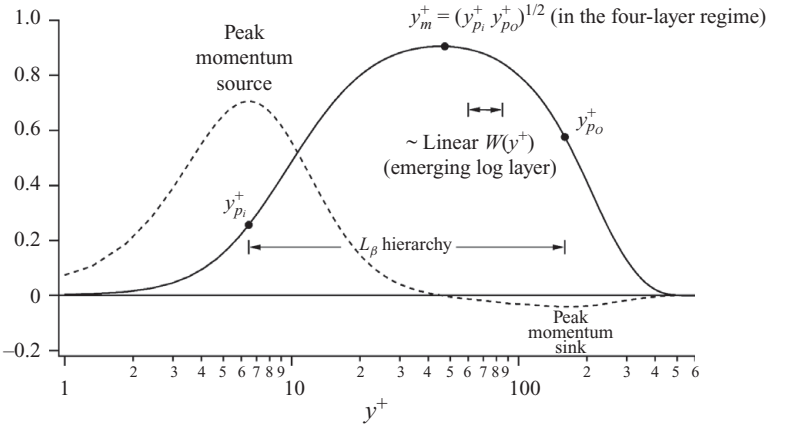


FIGURE 20. Features of the $-\overline{uv}^+$ (solid line) and $-\partial\overline{uv}^+/\partial y^+$ (dashed line) profiles relating to the properties of the L_β hierarchy. Note that the Reynolds-stress gradient profile is multiplied by a factor of 10 for clarity. Data are from the $\delta^+ = 367$ boundary layer of Wu & Moin (2009).

development stage, however, this process is relatively quickly constrained by the boundary conditions. At this point, the minimum and maximum lengths on the L_β hierarchy effectively define the inner and outer scales. The lower and upper limits of the hierarchy were previously estimated to respectively reside between $20 \lesssim y^+ \lesssim 36$ and $y/\delta \simeq 0.5$ (Fife *et al.* 2005*b*). Estimates from figure 13 put the smallest and largest layer widths to be about $10\nu/u_\tau$ and 0.27δ, respectively. The dynamical self-similarity that defines the L_β hierarchy exists owing to the relationship between the slope and curvature of the Reynolds stress profile (i.e. (1.12)) in the region between the two inflection points of the $-\overline{uv}^+$ profile. This dynamical self-similarity is required for (1.3) to admit a logarithmic mean profile (Fife *et al.* 2009). This fact also underpins the theoretically based estimate for λ in the relation $y_m^+ = \lambda\sqrt{\delta^+}$, i.e. $y_m^+ = \sqrt{y_{p_i}^+ y_{p_o}^+}$, see the discussion relating to figure 18.

Based upon the results herein, figure 20 indicates a lower bound for the L_β hierarchy that is slightly modified from its previous estimation. Specifically, a condition for the existence of the minimal $y_m^+(\beta)$ is that it corresponds to a position for which $-\partial^2\overline{uv}^+/\partial y^{+2}$ is negative and $-\partial\overline{uv}^+/\partial y^+$ is much less than (say, between 5 and 20 times smaller than) its maximal value of about 0.07 (see figure 16*b*). Values corresponding to 0.07/5 and 0.07/20 yield the $20 \lesssim y_m^+(\beta) \lesssim 36$ estimate cited above. When, however, an L_β layer having a width of about 10 viscous units is nominally centred about $y^+ = 20$, it extends to within only a few viscous units of $y^+ = 7$. The specification of this as the lower bound is given credence by the simple efficacy of (3.6). It is further reinforced by the fact that the meso-scaling of the Reynolds stress and mean velocity by Wei *et al.* (2005*b*) and Wei *et al.* (2007), respectively, and the logarithmic expansions about y_m^+ for the Reynolds stress and mean velocity by Sreenivasan & Bershadskii (2006) all effectively extend to within 7–11 viscous units from the wall (see also discussion in Klewicki 2010). Note that Sreenivasan & Bershadskii (2006) argue for logarithmic expansions about y_m^+ based upon 'the number of hierarchical scales up to the height y^+ in the wall layer is order $\ln y^+$'. The present theory reveals that this apt heuristic argument is also entirely consistent with the structure of the L_β hierarchy formally admitted by (1.3). (Note also that both in

https://doi.org/10.1017/jfm.2011.253 Published online by Cambridge University Press

channel and pipe flows it is analytically known that meso-scaling for the Reynolds stress transparently melds with outer scaling, Fife *et al.* 2005*b*, and thus the meso-scaling and logarithmic expansions are expected, as the data show, to be valid to the centreline.) Of course, this more precise specification of the lower limit of the L_β hierarchy has an inconsequential impact on the order-of-magnitude analyses that underlie the rest of the theory.

The results of figure 18 provide evidence that the primary mathematical attributes required for the development of a logarithmic mean velocity profile are established relatively early within the nonlinear development stage of the transitional regime. The emergence of logarithmic behaviour is expected to be most rapidly approximated on the interior, inertially dominated, sub-domain of the L_β hierarchy described in § 3.5.2. Figure 20 depicts this domain at $\delta^+ = 367$ in terms of the properties of the $-\overline{uv}^+$ and $-\partial\overline{uv}^+/\partial y^+$ profiles. The present observations reveal that the inner and outer lengths become relevant to scaling mean flow dynamics in the four-layer regime once the constraints posed by the boundary conditions of (1.3) on the mechanism of turbulent inertia effectively anchor the inner and outer peaks of $-\partial\overline{uv}^+/\partial y^+$ as described in § 3.5.3. The self-similar properties admitted by (1.3) indicate that the minimum and maximum scales of dynamically relevant motions (inner and outer scales) are connected across the $W(y^+)$ distribution of the L_β hierarchy. As indicated by figure 17, with increasing δ^+ the hierarchy spreads inwards and outwards from its central layer (layer III), such that, regardless of δ^+, $W(y^+)$ always spans the range $O(\nu/u_\tau)$ to $O(\delta)$. This structure is qualitatively distinct from that surmised by postulating the existence of an overlapping region, where the Reynolds stress is taken to be approximately constant, and where inner and outer representations are hypothesized to simultaneously hold.

4.3. *Summary*

To date, no DNS has computed the full transitional regime as initiated with infinitesimal disturbances. Thus, the present study necessarily explored flows whose instabilities are triggered by bypass mechanisms. As pointed out by one referee, a useful next step might be a detailed simulation, initiated by linear waves, that takes the flow up until the first part of the nonlinear stage, followed by another simulation that uses the first simulation as its flow condition.

With the stated proviso, the theoretical framework utilized herein provides a self-consistent physical/mathematical description of the mean dynamics in the transitional boundary layer. This description begins with the first appearance of a finite and positive $-\rho\overline{uv}(y)$ distribution in the boundary layer, and thereafter extends to arbitrary δ^+. The present results are similar to the previous findings for channel flow (Elsnab *et al.* 2011). The transitional regime is marked by a non-negligible influence of all three terms in (1.3) for $0 < y < \delta$. During the transitional regime, turbulent inertia, quantified in the mean by the Reynolds stress gradient, acts to rearrange the mean viscous force and mean advection profiles as depicted in figure 19. This culminates with the segregation of mean forces reflected in the four-layer structure of figure 1. The balance breaking and exchange of forces across layer III is a central attribute of this structure, as its overall appearance is replicated across the range of scales residing on the L_β hierarchy. The present results show that the emergence of the four-layer structure correlates with the formation of a linear zone in the $W(y^+)$ profile that underlies the emergence of a logarithmic mean profile. This occurs when the end points of the L_β hierarchy, as quantified in units of its intrinsic mean length scale ($\sqrt{\nu\delta/u_\tau}$), exceed a scale separation of about 0.75 decade below and above

https://doi.org/10.1017/jfm.2011.253 Published online by Cambridge University Press

$y_m \simeq 2\sqrt{\nu\delta/u_\tau}$ (see figure 17). An accurate estimation for the scaling behaviour of y_m^+ is then realized in (3.5) by simply using the asymptotic approximations for the end points of the L_β hierarchy.

We especially acknowledge the comments and suggestions of Professor Paul Fife. We thank the reviewers for their constructive comments and suggestions. We are also grateful to Drs Schlatter and Orlu and their colleagues for making their recent DNS data sets available on the internet, and similarly to Drs Hoyas, Jimenez, Laadhari and Kuroda. This work was partially supported by the Office of Naval Research grant N00014-08-1-0836, grant monitor Ron Joslin.

REFERENCES

Adrian, R. 2007 Hairpin vortex organization in wall turbulence. *Phys. Fluids* **19**, 041301.

Afzal, N. 1982 Fully developed turbulent flow in a pipe: an intermediate layer. *Ing.-Arch.* **52**, 355–377.

Antonia, R., Teitel, M., Kim, J. & Browne, L. 1992 Low-Reynolds-number effects in a fully developed turbulent channel flow. *J. Fluid Mech.* **236**, 579–605.

Bailey, S., Hultmark, M., Smits, A. & Schultz, M. 2008 Azimuthal structure of turbulence in high Reynolds number pipe flow. *J. Fluid Mech.* **615**, 121–138.

Balakumar, B. & Adrian, R. 2007 Large- and very-large-scale motions in channel and boundary-layer flows. *Phil. Trans. R. Soc. Lond.* A **365**, 665–681.

Buschmann, M., Indinger, T. & Gad-el-Hak, M. 2009 Near-wall behavior of turbulent wall-bounded flows. *Intl J. Heat Fluid Flow* **30**, 993–1006.

Ching, C. Y., Djendi, L. & Antonia, R. A. 1995 Low Reynolds-number effects in a turbulent boundary layer. *Exp. Fluids* **19**, 61–68.

Criminale, W., Jackson, T. & Joslin, R. 2003 *Theory and Computation in Hydrodynamic Stability*. Cambridge University Press.

Dean R. 1978 Reynolds number dependence of skin friction and other bulk flow variables in two-dimensional rectangular duct flow. *J. Fluids Engng* **100**, 215–223.

DeGraaff, D. B. & Eaton, J. K. 2000 Reynolds-number scaling of the flat-plate turbulent boundary layer. *J. Fluid Mech.* **422**, 319–346.

Elsnab, J., Klewicki, J., Maynes, D. & Ameel, T. 2011 Mean dynamics of transitional channel flow. *J. Fluid Mech.* **678**, 451–481.

Elsnab, J., Maynes, D., Klewicki, J. & Ameel, T. 2010 Mean flow structure in high aspect ratio microchannel flows. *Exp. Therm. Fluid Sci.* **34**, 1077–1088.

Eyink G. 2008 Turbulent flow in pipes and channels as cross-stream 'inverse cascades' of vorticity. *Phys. Fluids* **20**, 125101.

Fife, P., Klewicki, J., McMurtry, P. & Wei, T. 2005*a* Multiscaling in the presence of indeterminacy: wall-induced turbulence. *Multiscale Model. Simul.* **4**, 936–959.

Fife, P., Klewicki J. & Wei, T. 2009 Time averaging in turbulence settings may reveal an infinite hierarchy of length scales. *J. Discrete Continuous Dyn. Syst.* **24**, 781–807.

Fife, P., Wei, T., Klewicki, J. & McMurtry, P. 2005*b* Stress gradient balance layers and scale hierarchies in wall bounded turbulent flows. *J. Fluid Mech.* **532**, 165–189.

Ganapathisubramani, B. 2008 Statistical structure of momentum sources and sinks in the outer region of a turbulent boundary layer. *J. Fluid Mech.* **606**, 225–237.

Guala, M., Hommema, S. & Adrian, R. 2006 Large-scale and very-large-scale motions in turbulent pipe flow. *J. Fluid Mech.* **554**, 521–542.

Hoyas, S. & Jimenez, J. 2006 Scaling the velocity fluctuations in turbulent channels up to $Re_\tau = 2003$. *Phys. Fluids* **18**, 011702.

Jordinson, R. 1970 The flat plate boundary layer. Part 1. Numerical integration of the Orr–Sommerfeld equation. *J. Fluid Mech.* **43**, 801–811.

Klewicki, J. 2010 Reynolds number dependence, scaling, and dynamics of turbulent boundary layers. *J. Fluids Engng* **132**, 094001.

https://doi.org/10.1017/jfm.2011.253 Published online by Cambridge University Press

Klewicki, J., Fife, P. & Wei, T. 2009 On the logarithmic mean profile. *J. Fluid Mech.* **638**, 73–93.

Klewicki, J., Fife, P., Wei, T. & McMurtry, P. 2007 A physical model of the turbulent boundary layer consonant with mean momentum balance structure. *Phil. Trans. R. Soc. Lond.* A **365**, 823–839.

Kuroda, A., Kasagi, N. & Hirata, M. 1989 A direct numerical simulation of the fully developed turbulent channel flow. In *Proc. Intl Symp. on Computational Fluid Dynamics*, Nagoya, Japan, pp. 1174–1179.

Laadhari, F. 2002 On the evolution of maximum turbulent kinetic energy production in a channel flow. *Phys. Fluids* **14**, L65–L68.

Long, R. & Chen, T.-C. 1981 Experimental evidence for the existence of the mesolayer in turbulent systems. *J. Fluid Mech.* **105**, 19–59.

Marusic, I. 2009 Unraveling turbulence near walls. *J. Fluid Mech.* **630**, 1–4.

Metzger, M., Adams, P. & Fife, P. 2008 Mean momentum balance in moderately favourable pressure gradient turbulent boundary layers. *J. Fluid Mech.* **617**, 107–140.

Monkewitz, P., Chauhan, K. & Nagib, H. 2008 Comparison of mean flow similarity laws in zero-pressure-gradient turbulent boundary layers. *Phys. Fluids* **20**, 105102.

Monty, J., Stewart, J., Williams, R. & Chong, M. 1981 Large scale features in turbulent pipe and channel flows. *J. Fluid Mech.* **589**, 147–156.

Nagib, H. & Chauhan, K. 2008 Variation of von Kármán coefficient in canonical flows. *Phys. Fluids* **20**, 101518.

Nagib, H., Chauhan, K. & Mokewitz, P. 2007 Approach to an asymptotic state for zero pressure gradient turbulent boundary layers. *Phil. Trans. R. Soc. Lond.* A **365**, 755–770.

Osterlund, J., Johansson, A., Nagib, H. & Hites, M. 2000 A note on the overlap region in turbulent boundary layers. *Phys. Fluids* **12**, 1–4.

Perry, A. & Chong, M. 1982 On the mechanism of wall turbulence. *J. Fluid Mech.* **119**, 173–217.

Perry, A. & Marusic, I. 1995 A wall-wake model for the turbulence structure of boundary layers. Part 1. Extension of the attached eddy hypothesis. *J. Fluid Mech.* **298**, 361–388.

Schlatter, P. & Orlu, R. 2010 Assessment of direct numerical simulation data of turbulent boundary layers. *J. Fluid Mech.* **659**, 116–126.

Schlichting, H. & Gersten, K. 2000 *Boundary Layer Theory*. Springer.

Schoppa, W. & Hussain, F. 2002 Coherent structure generation in near-wall turbulence. *J. Fluid Mech.* **453**, 57–108.

Sherman, F. 1990 *Viscous Flows*. McGraw-Hill.

Smits, A., McKeon, B. & Marusic, I. 2011 High Reynolds number wall turbulence. *Annu. Rev. Fluid Mech.* **43**, 253–375.

Sreenivasan, K. 1989 The turbulent boundary layer. In *Frontiers in Experimental Fluid Mechanics* (ed. M. Gad-el-Hak), pp. 159–209. Springer.

Sreenivasan, K. & Bershadskii, A. 2006 Finite-Reynolds-number effects in turbulence using logarithmic expansions. *J. Fluid Mech.* **554**, 477–498.

Sreenivasan, K. & Sahay, A. 1997 The persistence of viscous effects in the overlap region and the mean velocity in turbulent pipe and channel flows. In *Self-Sustaining Mechanisms of Wall Turbulence* (ed. R. Panton), pp. 253–272. Computational Mechanics Publications.

Tomkins, C. & Adrian R. 2003 Spanwise structure and scale growth in turbulent boundary layers. *J. Fluid Mech.* **490**, 37–74.

Townsend, A. 1976 *The Structure of Turbulent Shear Flow*. Cambridge University Press.

Waleffe, F. 1997 On a self-sustaining process in shear flows. *Phys. Fluids* **7**, 883–900.

Wei, T., Fife, P. & Klewicki, J. 2007 On scaling the mean momentum balance and its solutions in turbulent Couette–Poiseuille flow. *J. Fluid Mech.* **573**, 371–398.

Wei, T., Fife, P., Klewicki, J. & McMurtry, P. 2005*a* Properties of the mean momentum balance in turbulent boundary layer, pipe and channel flows. *J. Fluid Mech.* **522**, 303–327.

https://doi.org/10.1017/jfm.2011.253 Published online by Cambridge University Press

Wei, T., McMurtry, P., Klewicki, J. & Fife, P. 2005*b* Mesoscaling of the Reynolds shear stress in turbulent channel and pipe flows. *AIAA J.* **43**, 2350–2353.

Wu, X. 2010 Establishing the generality of three phenomena using a boundary layer with free-stream passing wakes. *J. Fluid Mech.* **664**, 193–219.

Wu, X. & Moin, P. 2009 Direct numerical simulation of turbulence in a nominally zero-pressure-gradient flat-plate boundary layer. *J. Fluid Mech.* **630**, 5–41.

Wu, X. & Moin, P. 2010 Transitional and turbulent boundary layer with heat transfer. *Phys. Fluids* **22**, 085105.

https://doi.org/10.1017/jfm.2011.253 Published online by Cambridge University Press